Research Square

Preprints are preliminary reports that have not undergone peer review.
They should not be considered conclusive, used to inform clinical practice,
or referenced by the media as validated information.

Outer-Edge Impedance Mismatch Controls the High-Order Near-Field Floor and Repair of Approximate Mechanical Cloaks

Guangtao Wei

wgt@hrbeu.edu.cn

Fujian Agriculture and Forestry University https://orcid.org/0000-0001-8266-9776

Miao Yu

Fujian Agriculture and Forestry University

Jun Liu

Fujian Provincial Cancer Hospital

Research Article

Keywords:

Posted Date: November 25th, 2026

DOI: https://doi.org/10.21203/rs.3.rs-11850505/v1

License: This work is licensed under a Creative Commons Attribution 4.0 International License.
Read Full License

Additional Declarations: The authors declare no competing interests.

Outer-Edge Impedance Mismatch Controls the High-Order Near-Field Floor and Repair of Approximate Mechanical Cloaks

Guangtao Wei[1,*], Miao Yu[1], Jun Liu[2,*]

[1] College of Mechanical and Electrical Engineering, Fujian Agriculture and Forestry University, Fuzhou 350002, Fujian, China.

[2] Department of Medical Oncology, Clinical Oncology School of Fujian Medical University, Fujian Cancer Hospital, Fuzhou 350000, Fujian, China.

[*] *Corresponding authors: Guangtao Wei (E-mail: wgt@hrbeu.edu.cn); Jun Liu (E-mail: 344196244@qq.com).*

Abstract

An approximate mechanical cloak can pass a strict worst-case boundary test yet still amplify the disturbance from a nearby load well above the incremental acceptance tolerance τ. Here, we uncover the spectral mechanism behind this failure, predict it without fitted parameters, and demonstrate how to repair it directly at the outer boundary. Because regular elastostatic fields decay inward from a source at radius $r_{\mathrm{src}} > b$ as $(b/r_{\mathrm{src}})^{n-1}$, boundary tests strongly filter out high angular harmonics n and leave impedance jumps at the outer edge unconstrained. While scattering from a bare void decays exponentially at rate $4\ln(a_0/b)$ with an n^4 prefactor, any mismatched isotropic outer layer approaches a finite, closed-form reflection floor (e_1, e_2). We show that an exact scalar analogue also governs 2D steady conduction. Conversely, a compliance-matched polar-orthotropic ring leaves both background solution subspaces invariant for all $n \geq 2$, completely eliminating this high-order floor ($h_\infty = 0$). Independent finite-element checks—using a 567,938-DOF quadratic triangular mesh and a 2,883-DOF discrete beam model—confirm our zero-parameter predictions ($0.990-1.026\times$) and demonstrate localized patch failure up to 150.7τ. Crucially, adding a $2.5\mathrm{mm}$ outer buffer trained solely on boundary loads reduces near-field error by $48.6\times$ ($148.0\tau \rightarrow 3.05\tau$), establishing a general interface-continuity rule for inverse-designed metamaterials.

Introduction

Transformation optics, acoustics, and elastodynamics provide an exact geometric framework for shielding objects from external fields [1–8]. In elastostatics, however, exact transformation cloaks generally require singular, asymmetric, or generalized Cosserat constitutive tensors at the inner boundary [3, 7]. To obtain manufacturable designs for planar plates and architected lattices, recent experimental and numerical studies have moved from pentamode and direct-lattice transformations [9–12] toward *approximate* elastostatic cloaks. These cloaks are created through topology optimization, aperiodic data-driven synthesis, structural disorder, or spinodal micro-architectures trained on finite sets of external boundary loads—including uniaxial, biaxial, pure-shear, compatible-boundary, and worst-case minimax boundary conditions [13–18]. In particular, Senhora, Sanders, and Paulino [18] showed that training on a small set of hand-picked loads introduces directional bias; to overcome this, they developed a sequential two-stage framework that identifies worst-case boundary loads and minimizes the summed energy mismatch across them. Within the external boundary-loaded regimes for which they are designed, such manufacturable cloaks effectively suppress exterior field disturbances.

Even when a cloak is *unbiased* across all external boundary loads, however, a fundamental spectral question remains open: *Why do boundary-validated cloaks still fail by orders of magnitude under localized exterior near-field forces, how can this per-order breakdown be predicted without fitted parameters, and what outer-boundary conditions eliminate the high-order failure floor?* In electromagnetism, acoustics, and inverse problems, related bounds and non-uniqueness in passive cloaking have been studied using causality sum rules [19], scattering cancellation [20], Calderón-type inverse non-uniqueness [21, 22], generalized polarization tensors (GPTs) [23], and classical neutral-inclusion theory [24–28].

Compared with pre-stressed hyperelastic transformation cloaks [29] and uniform-field neutral-inclusion coatings [28], our formulation and theoretical results differ in four concrete ways. First, regarding the *constitutive and geometric setting*, we remain strictly within classical linear elasticity without finite pre-stress or Cosserat terms, and we construct an explicit family of concentric polar-orthotropic rings rather than posing an abstract inverse boundary problem. Second, regarding *harmonic scope*, classical neutral inclusions cancel scattering only under uniform hydrostatic ($n = 0$) or shear ($n = 2$) loading; by contrast, our compliance-matched polar-orthotropic ring leaves both regular and decaying background subspaces invariant at *every* angular order $n \geq 2$ (and leaves regular subspaces invariant at $n = 0,1$) for any finite ring thickness. Third, regarding the *role of an inner void*, placing our ring around a traction-free void eliminates the outer-interface reflection floor ($h_\infty = 0$) while still transmitting modified void multipoles. Fourth, in the *near-field loading regime*, our analysis clarifies how the source radius r_{src}, radial half-width w, angular patch width $\Delta\theta$, and outer-edge stiffness continuity jointly govern the competition between the high-order reflection floor and residual low-order hole scattering.

Here, we establish a unified framework within classical linear elasticity that connects the **per-order reflection floor**, **zero-parameter quantitative prediction**, and **outer-edge-matched repair**. Building on prior work that addressed few-load bias and worst-case external-boundary minimax training [18], we organize our contributions around three analytical and constructive advances:

1. **Per-order spatial filtering and the exact high-order reflection floor.** In Results Section 1, we prove analytically that scattering from a bare void decays exponentially at rate $\lim_{n\to\infty} n^{-1}\ln v_n = 4\ln(a_0/b)$—specifically, $v_n \sim \kappa_0^{-1}(1-q^2)^4 n^4 q^{4n-4}$ and $\|\boldsymbol{S}_V(n)\|_2 \sim \kappa_0^{-1}(1-q^2)^2 n^2 q^{2n-2}$ for $q = a_0/b$. In contrast, any isotropic outer cloak layer whose moduli differ from the background ($(\mu_L, K_L) \neq (\mu_0, K_0)$) approaches a non-vanishing flat-interface reflection floor (e_1, e_2) as $n \to \infty$. An exact scalar counterpart of this floor also appears in 2D steady thermal conduction [30–32]. Because regular fields propagating inward from a source at radius r_{src} decay as $(b/r_{\mathrm{src}})^{n-1}$, standard boundary tests naturally filter out high-n harmonics and overlook this floor. Conversely, thin or localized near-field loads applied close to $r = b$ excite it directly.
2. **All-order neutral polar-orthotropic rings and exact harmonic scope.** Extending the half-plane impedance formalism of Stroh and Suo [33–36] using symbolic algebra and exact rational arithmetic, we prove that a polar-orthotropic ring satisfying two compliance-matching conditions within the positive-definite window $(1-\nu_0)/2 < n_S < 2/(1-\nu_0)$ leaves both regular and decaying background solution subspaces invariant at *every* harmonic order $n \geq 2$ (and leaves the regular subspaces invariant at $n = 0,1$). This theorem establishes a clear distinction between a neutral ring embedded in an intact background—which produces zero scattering at all n—and a ring surrounding a void, where the high-order reflection floor vanishes ($h_\infty = 0$) while low- and intermediate-order hole scattering remains active.

3. **Zero-parameter coupled prediction, localized patch and discrete-beam lattice validation, and outer-edge repair without near-field training.** By incorporating angular Toeplitz mode coupling, our theory quantitatively predicts independent 6-node quadratic triangular (T6) finite-element benchmarks up to 567,938 degrees of freedom (DOFs) across radial scales and angular cutoffs, with no fitted parameters. Crucially, eliminating outer-edge impedance mismatch—via a background buffer, a smooth cosine taper, or a compliance-matched polar-orthotropic shell—removes the high-order floor ($h_\infty = 0$) and reduces thin-source deterioration by $48.6\times$ ($148.0\tau \to 3.05\tau$) *using boundary loads alone*. This analysis also clarifies the Pareto trade-off between strict all-mode non-deterioration and strong low-order shielding.

To test realistic localized loading, we evaluate these fixed unbuffered and buffered boundary-repaired designs under self-equilibrated finite-arc force patches ($\Delta\theta = 2^\circ - 30^\circ$, stand-off distance $d = 0-8\text{mm}$) on the 567,938-DOF T6 mesh. These tests confirm that compact contact loads excite high-order reflections up to 150.7τ (with 0.990–1.005× FE-to-theory agreement for $\Delta\theta \le 15^\circ$), which a 2.5mm outer buffer suppresses by $> 1{,}400\times$ at $\Delta\theta = 4^\circ$. We further develop geometry-tolerant, bounded-stiffness designs that remain effective across four hole shapes, and we directly verify both the outer-edge mismatch jump and discrete buffering recovery in 2D Timoshenko and Euler–Bernoulli beam finite-element models of square-lattice cloaks (961 nodes, 2,883 DOFs, 564 cloak struts). Taken together, these results establish a general interface-continuity principle for inverse-designed elastic, thermal, and wave metamaterials trained solely on boundary data.

Results

1. Per-angular-order transfer theory and the exact high-order reflection floor

Consider a circular plate of radius $R_{\text{out}} = 75\text{mm}$ (or a $150\text{mm} \times 150\text{mm}$ square plate in our T6 finite-element [FE] validation) made of a 2D planar isotropic, linear-elastic background medium $\mathcal{M}_0$. The background is characterized by its planar area bulk modulus $K_0 = (C_{11}^{(0)} + C_{12}^{(0)})/2$, shear modulus $\mu_0 = C_{66}^{(0)} = (C_{11}^{(0)} - C_{12}^{(0)})/2$, **2D planar isotropic effective Poisson ratio** $\nu_0 = C_{12}^{(0)}/C_{11}^{(0)} \in (-1,1)$, and 2D Kolosov constant $\kappa_0 = 1 + 2\mu_0/K_0 = (3-\nu_0)/(1+\nu_0)$. Throughout this study, we examine three thermodynamically positive-definite 2D elastic backgrounds ($K_0 > 0, \mu_0 > 0 \Leftrightarrow -1 < \nu_0 < 1$): $\nu_0 = 0.60$ ($\kappa_0 = 1.500$), an auxetic medium $\nu_0 = -0.80$ ($\kappa_0 = 19.000$ [37]), and a conventional medium $\nu_0 = 0.33$ ($\kappa_0 = 2.008$). Physically, $\nu_0 = 0.60$ corresponds exactly to the 2D plane-strain cross-sectional response of a 3D isotropic solid with $\nu_{3\text{D}} = \nu_0/(1+\nu_0) = 0.375$ (or to a 2D architected isotropic cellular plate), whereas $\nu_0 = 0.33$ and $\nu_0 = -0.80$ correspond directly to 3D plane-stress elastic sheets ($\nu_{3\text{D}} = \nu_0 \in (-1,0.5)$).

A central circular void of radius $a_0 = 30\text{mm}$ is surrounded by an annular cloak occupying $a_0 \le r \le b$ ($b = 55\text{mm}$), which is divided into 20 concentric layers of thickness 1.25mm. We apply either an external boundary load or an exterior body-force distribution $\boldsymbol{f}(\boldsymbol{x})$ supported in $\Omega_{\text{obs}} = \{r > b\}$, normalized so that the intact-plate elastic input energy is $\mathcal{E}_0(\boldsymbol{f}) = \frac{1}{2}\boldsymbol{F}^{\mathrm{T}}\boldsymbol{K}_0^{-1}\boldsymbol{F} = 1$. To measure the exterior disturbance of the scattered displacement field $\boldsymbol{w}_X = \boldsymbol{u}_X - \boldsymbol{u}_0$ ($X \in \{C, V\}$, representing the cloaked plate and bare void, respectively), we evaluate the **exterior symmetric elastic strain-energy** integral:

$$\mathcal{E}_{\text{err},X}(\boldsymbol{f}) = \frac{1}{2}\int_{\Omega_{\text{obs}}} \boldsymbol{\varepsilon}(\boldsymbol{w}_X) : \boldsymbol{C}_0 : \boldsymbol{\varepsilon}(\boldsymbol{w}_X)\, \mathrm{d}A = -\frac{1}{2}\int_{r=b} \boldsymbol{w}_X \cdot (\boldsymbol{\sigma}_0(\boldsymbol{w}_X)\boldsymbol{n})\, \mathrm{d}s,$$

where $\boldsymbol{\varepsilon}(\boldsymbol{w}_X) = \frac{1}{2}(\nabla \boldsymbol{w}_X + \nabla \boldsymbol{w}_X^{\mathrm{T}})$ is the symmetric linearized strain tensor (which vanishes identically for infinitesimal rigid-body translations and rotations), $\boldsymbol{\sigma}_0(\boldsymbol{w}_X) = \boldsymbol{C}_0 : \boldsymbol{\varepsilon}(\boldsymbol{w}_X)$ is the corresponding stress, and $\boldsymbol{n}$ is the outward unit normal to the cloak disc $r \le b$ (see Supplementary Note 1 and Supplementary Table S0 for canonical definitions). Because $\boldsymbol{w}_X$ is unforced inside Ω_{obs} whenever loads act on the outer boundary or strictly in the exterior region, Clapeyron's theorem equates this exterior area integral to the boundary work along $r = b$. Note that any constant factor of 2 in discrete quadratic forms $\boldsymbol{w}_X^{\mathrm{T}} \boldsymbol{K}_{\mathrm{out}} \boldsymbol{w}_X$ cancels identically in all normalized ratios. Normalizing by the bare-hole reference visibility $\ell_V = \sup_{\boldsymbol{f} \in \mathcal{L}_{\mathrm{BD}}, \mathcal{E}_0(\boldsymbol{f})=1} \mathcal{E}_{\mathrm{err},V}(\boldsymbol{f})$ over the boundary-displacement space $\mathcal{L}_{\mathrm{BD}}$, we track *both* the incremental deterioration relative to the bare hole and the total cloak error over any load space $\mathcal{L}$:

$$h(\mathcal{L}) = \sup_{\boldsymbol{f} \in \mathcal{L}, \mathcal{E}_0(\boldsymbol{f})=1} \frac{\mathcal{E}_{\mathrm{err},C}(\boldsymbol{f}) - \mathcal{E}_{\mathrm{err},V}(\boldsymbol{f})}{\ell_V}, \quad E_{\max,C}(\mathcal{L}) = \sup_{\boldsymbol{f} \in \mathcal{L}, \mathcal{E}_0(\boldsymbol{f})=1} \frac{\mathcal{E}_{\mathrm{err},C}(\boldsymbol{f})}{\ell_V}. \tag{1}$$

Tracking $E_{\max,C}(\mathcal{L})$ together with $h(\mathcal{L})$ ensures genuine cloaking rather than trivial non-deterioration: leaving the hole completely uncloaked gives $h \equiv 0$ identically, yet leaves $E_{\max,C} = 1$. We say that a cloak passes incremental acceptance on $\mathcal{L}$ at tolerance τ if $h(\mathcal{L}) \le \tau$.

For an axisymmetric or cylindrically orthotropic layered cloak at angular harmonic $n \ge 1$, we expand the displacements as $(u_r, u_\theta) = (U_n(r)\cos n\theta, V_n(r)\sin n\theta)$ and the radial tractions as $(r\sigma_{rr}, r\sigma_{r\theta}) = (r\Sigma_{rr,n}\cos n\theta, r\Sigma_{r\theta,n}\sin n\theta)$. In terms of the logarithmic radius $s = \ln r$, the elastostatic state vector $\boldsymbol{y}_n(s) = [U_n, V_n, r\Sigma_{rr,n}, r\Sigma_{r\theta,n}]^{\mathrm{T}}$ satisfies the linear first-order system $\mathrm{d}\boldsymbol{y}_n/\mathrm{d}s = \boldsymbol{N}_n \boldsymbol{y}_n$ within each homogeneous layer (Fig. 1a). (At $n = 0$, the axisymmetric radial expansion mode and the torsional rotation mode $u_\theta(r)$ decouple into two rank-2 subsystems, as detailed in Supplementary Note 2.) Scattering at the outer cloak interface $r = b$ is governed by 2×2 Dirichlet-to-Neumann (DtN) impedance matrices: the intact interior impedance $\boldsymbol{Z}_{\mathrm{in}}(n)$ ($r\boldsymbol{\Sigma}_n = +\boldsymbol{Z}_{\mathrm{in}}\boldsymbol{u}_n$), the exterior impedance $\boldsymbol{Z}_{\mathrm{ext}}(n, b)$ ($r\boldsymbol{\Sigma}_n = -\boldsymbol{Z}_{\mathrm{ext}}\boldsymbol{u}_n$), the cloak impedance $\boldsymbol{Z}_C(n)$ propagated outward from $\boldsymbol{Z}(a_0) = \boldsymbol{0}$ via Möbius Riccati updates, and the bare-hole impedance $\boldsymbol{Z}_V(n)$ propagated through the background material across $[a_0, b]$. Incident displacement traces on $r = b$ then map to scattered traces according to

$$\boldsymbol{S}_X(n) = (\boldsymbol{Z}_X(n) + \boldsymbol{Z}_{\mathrm{ext}}(n, b))^{-1}(\boldsymbol{Z}_{\mathrm{in}}(n) - \boldsymbol{Z}_X(n)), \quad X \in \{C, V\}, \tag{2}$$

The corresponding per-order deterioration operator acting on incident traces at $r = b$—where the exterior strain energy per unit mode is $\frac{\pi}{2}\boldsymbol{w}_n^{\mathrm{T}}\boldsymbol{Z}_{\mathrm{ext}}\boldsymbol{w}_n$ for $n \ge 1$ (which is normalized by ℓ_V when forming Eq. (1))—is given by

$$\boldsymbol{M}_n = \boldsymbol{S}_C(n)^{\mathrm{T}}\boldsymbol{Z}_{\mathrm{ext}}(n, b)\boldsymbol{S}_C(n) - \boldsymbol{S}_V(n)^{\mathrm{T}}\boldsymbol{Z}_{\mathrm{ext}}(n, b)\boldsymbol{S}_V(n). \tag{3}$$

Taking the short-wavelength (flat-interface) limit $n \to \infty$ yields two exact asymptotic laws, which are derived in Methods and Supplementary Note 1:

- **Bare-hole exponential decay:** For a bare void ($q = a_0/b < 1$), propagating incident modes inward to the traction-free wall $r = a_0$ and back to $r = b$ produces an n^2 algebraic prefactor in the displacement scattering norm, $\|\boldsymbol{S}_V(n)\|_2 \sim \frac{(1-q^2)^2}{\kappa_0}\, n^2 q^{2n-2} \to 0$, and an n^4 prefactor in the unit-incident-disc-energy error baseline: $v_n \sim \frac{(1-q^2)^4}{\kappa_0}\, n^4 q^{4n-4}$, with exponential decay rate $\lim_{n\to\infty} n^{-1}\ln v_n = 4\ln q$. We verified this law using 140-digit arbitrary-precision arithmetic on the $v_0 = 0.60$ background ($q = 30/55$, $\kappa_0 = 1.500$, theoretical prefactor $(1 - q^2)^4/\kappa_0 = 0.16235$). Here, v_n decays rapidly to 3.90×10^{-28} ($3.89928 \times$

10^{-28}) at $n = 32$, 1.26×10^{-60} at $n = 64$, and 8.18×10^{-127} at $n = 128$; meanwhile, the scaled ratio $v_n/(n^4 q^{4n-4}) = \{0.16305, 0.16252, 0.16239\}$ converges cleanly to 0.16235 (gray dashed curve in Fig. 1b).

- **Cloak outer-layer reflection floor:** Consider any cloak whose outermost layer has thickness $\Delta r_{\text{out}} \gg b/n$ and general isotropic moduli (μ_L, K_L) with Kolosov constant $\kappa_L = 1 + 2\mu_L/K_L$. Reflections from buried interfaces ($r \le b - \Delta r_{\text{out}}$) decay **exponentially** in $n\Delta r_{\text{out}}/b$, so the cloak impedance $\boldsymbol{Z}_C(n)$ converges exponentially fast to the regular impedance $\boldsymbol{Z}_L^+(n)$ of medium L. In contrast, for a homogeneous disc or an unbounded exterior of finite radius b, direct evaluation on the exact background eigenvectors gives $\boldsymbol{Q}^{\mathrm{T}}\boldsymbol{Z}_{\text{in}}(n)\boldsymbol{Q} = 2\mu_0 \mathrm{diag}(n-1, (n+1)/\kappa_0)$ and $\boldsymbol{Q}^{\mathrm{T}}\boldsymbol{Z}_{\text{ext}}^{\infty}(n,b)\boldsymbol{Q} = 2\mu_0 \mathrm{diag}((n-1)/\kappa_0, n+1)$ (Methods 2). Consequently, $\boldsymbol{Z}_{\text{in}}(n)/n$ and $\boldsymbol{Z}_{\text{ext}}(n,b)/n$ converge to their half-plane limits only **algebraically**, with $O(1/n)$ curvature corrections (and the same convergence holds for finite R_{out} up to $O((b/R_{\text{out}})^{2n})$):

$$\lim_{n\to\infty} \frac{\boldsymbol{Z}_{\text{in}}(n)}{n} = \mu_0 \begin{bmatrix} 1+\kappa_0^{-1} & -(1-\kappa_0^{-1}) \\ -(1-\kappa_0^{-1}) & 1+\kappa_0^{-1} \end{bmatrix}, \quad \lim_{n\to\infty} \frac{\boldsymbol{Z}_{\text{ext}}(n,b)}{n} = \mu_0 \begin{bmatrix} 1+\kappa_0^{-1} & +(1-\kappa_0^{-1}) \\ +(1-\kappa_0^{-1}) & 1+\kappa_0^{-1} \end{bmatrix}. \tag{4}$$

These leading half-plane impedances share the same orthogonal eigenvectors $\boldsymbol{v}_{\pm} = \frac{1}{\sqrt{2}}[1, \pm 1]^{\mathrm{T}}$, but with swapped eigenvalues $(2\mu_0/\kappa_0, 2\mu_0)$ versus $(2\mu_0, 2\mu_0/\kappa_0)$. Substituting these leading $O(n)$ asymptotes into Equation (2) therefore diagonalizes the incident-energy-normalized scattering operator $\boldsymbol{Z}_{\text{in}}^{-1/2}\boldsymbol{S}_C^{\mathrm{T}}\boldsymbol{Z}_{\text{ext}}\boldsymbol{S}_C\boldsymbol{Z}_{\text{in}}^{-1/2}$ in the $\boldsymbol{v}_{\pm}$ basis, yielding two exact reflection-floor eigenvalues:

$$e_1 = \frac{\kappa_0(\mu_L - \mu_0)^2}{(\kappa_0\mu_L + \mu_0)^2}, \quad e_2 = \frac{(\mu_L\kappa_0 - \mu_0\kappa_L)^2}{\kappa_0(\mu_L + \mu_0\kappa_L)^2}. \tag{5}$$

Equivalently, we can express Equation (5) in terms of the classical bimaterial Dundurs parameters (α, β) ([38]; derived explicitly in Supplementary Note 1). This yields the exact asymmetric interface identity

$$e_1 = \kappa_0 \left(\frac{\alpha-\beta}{1+\beta}\right)^2, \quad e_2 = \frac{1}{\kappa_0}\left(\frac{\alpha+\beta}{1-\beta}\right)^2,$$

which directly links high-order reflection in mechanical cloaks to classical bimaterial interface mechanics. For simple scalar stiffness scaling $\boldsymbol{C}_L = a_{\text{out}}\boldsymbol{C}_0$ ($\mu_L = a_{\text{out}}\mu_0$, $\kappa_L = \kappa_0$), Equation (5) simplifies to $e_1 = \kappa_0(a_{\text{out}} - 1)^2/(\kappa_0 a_{\text{out}} + 1)^2$ and $e_2 = \kappa_0(a_{\text{out}} - 1)^2/(a_{\text{out}} + \kappa_0)^2$. To validate this closed-form result, we compared Equation (5) against numerical state-space transfer calculations at $n = 160$ across two test sets: 8 general isotropic (μ_L, K_L) pairs on $\nu_0 = 0.60$ ($\kappa_0 = 1.500$, yielding 13 nonzero eigenvalues since three shear- or bulk-matched pairs give $e_{\min} = 0$) and 18 scalar-contrast cases spanning all three backgrounds (36 eigenvalues). The analytical formula matches the numerical results to a maximum relative error of $\le 8.19 \times 10^{-11}$ overall, and $\le 1.20 \times 10^{-12}$ across the general pairs (Fig. 1c and Table 1).

Next, we examine the pressed-interface limit by letting $r_c \to b^+$ first—or equivalently, letting the radial half-width $w \to 0^+$ at $r_{\min} = b$ for the radial hat function $\psi(r; r_c, w) = \max(0, 1 - |r - r_c|/w)$ (Methods 5). In this limit, the boundary admittance behaves as $\boldsymbol{Y}_n(b) = (\boldsymbol{Z}_{\text{in}}(n) + \boldsymbol{Z}_{\text{ext}}(n,b))^{-1} \sim [2n\mu_0(\kappa_0+1)/\kappa_0]^{-1}\boldsymbol{I}_2$. Subsequently letting $n \to \infty$ yields the **pressed-source high-order floor**:

$$h_\infty = \lim_{n\to\infty} \lim_{r_c \to b^+} h_n(r_c) = \frac{\max(\kappa_0 e_1, e_2)}{(\kappa_0+1)\,\ell_V}. \tag{6}$$

Away from the pressed-interface limit, high-order scattering decays via two distinct mechanisms depending on the radial support of the source. First, (i) for any source with a positive stand-off clearance $r_{\min} > b$ (such as an idealized shell at $r_c > b$), inward elastostatic decay acts as an **exponential** high-n filter scaling as ~

$(b/r_{\min})^{2n-2}$ once $n(r_{\min}-b)/b \gg 1$, forcing $\lim_{n\to\infty} h_n = 0$. Second, (ii) for a fixed-width, fixed-shape radial hat whose support touches $r = b$ ($r_{\min} = b$, with linear ramp $\psi(r) \propto r - b$), integrating $(b/r)^{n-1}$ over $[b, b+2w]$ produces **algebraic** high-n decay once $n \gg b/w$—which also forces $\lim_{n\to\infty} h_n(w) = 0$. Across lower harmonics ($n \lesssim b/w$, for example $b/w = 352$ when $w = 0.15625$mm), however, the response remains close to the pressed-source plateau. In both regimes, distant boundary tests strongly suppress $n \gg 1$ and leave (e_1, e_2) effectively unpenalized, whereas concentrated near-field loads adjacent to $r = b$ excite h_∞ directly.

This spatial-harmonic filtering mechanism is not unique to vector elasticity; an exact scalar analogue occurs in 2D steady conduction ($\nabla\cdot(\sigma\nabla\varphi) = 0$; purple curve in Fig. 1b; cf. [31, 32]). Consider an insulating circular void ($r < a_0 = 30$mm, $\sigma_c = 0$) surrounded by a homogeneous cloaking shell ($a_0 < r < b = 55$mm) with conductivity ratio $\sigma_L/\sigma_0 = (b^2 + a_0^2)/(b^2 - a_0^2) = 157/85 \approx 1.8471$. Although this choice cancels the far-field dipole identically ($r_1 = 0$), all higher multipoles still reflect with coefficients

$$r_n = -\frac{(a_0/b)^2 - (a_0/b)^{2n}}{1-(a_0/b)^{2n+2}} \xrightarrow{n\to\infty} -\left(\frac{a_0}{b}\right)^2 = -\frac{36}{121} \approx -0.2975. \tag{7}$$

Under unit incident-disc energy normalization ($\boldsymbol{Z}_{\text{in}}^{-1}$, the common basis used for all curves in Fig. 1b), this conduction cloak approaches a plateau of $(a_0/b)^4 \approx 8.85\times10^{-2}$. When evaluated under pressed-interface source input-energy normalization ($Y_b = (\boldsymbol{Z}_{\text{in}} + \boldsymbol{Z}_{\text{ext}})^{-1}$) and the bare-hole reference ℓ_V^{cond}, it produces a pressed-ring deterioration floor of $h_\infty^{\text{cond}} = \frac{1}{2}(a_0/b)^4/\ell_V^{\text{cond}} = 1.7601$ —which is $3.61\times$ larger than the boundary worst case $h_{\text{BD}} = 0.4877$.

2. All-order neutral polar-orthotropic rings: exact invariance, stability window, and scope

In isotropic elasticity, eliminating the reflection floor ($e_1 = e_2 = 0$) uniquely requires matching both background moduli ($\mu_L = \mu_0$ and $\kappa_L = \kappa_0$). If we relax isotropy to polar orthotropy (with moduli $C_{rr}, C_{\theta\theta}, C_{r\theta}, G_{r\theta}$ aligned to polar coordinates (r,θ)), however, a two-parameter material family shares the exact half-plane Stroh/Barnett–Lothe impedance of the isotropic background [33–36]. Expressed in terms of plane compliances $(s_{11}, s_{22}, s_{12}, s_{66})$ with $s_{11} = s_{22}$ and a dimensionless scaling parameter $n_S > 0$, choosing

$$s_{11}^{(m)} = s_{22}^{(m)} = \frac{s_{11}^{(0)}}{n_S},\quad s_{12}^{(m)} = s_{11}^{(0)} + s_{12}^{(0)} - s_{11}^{(m)},\quad s_{66}^{(m)} = 2(2n_S^2 - 1)s_{11}^{(m)} - 2s_{12}^{(m)} \tag{8}$$

matches the background flat-interface impedance as $n \to \infty$. Crucially, the material defined by Equation (8) is thermodynamically admissible—meaning its stiffness tensor $\boldsymbol{C}^{(m)}$ is positive definite ($C_{rr}^{(m)} > |C_{r\theta}^{(m)}|$ and $G_{r\theta}^{(m)} > 0$)—if and only if

$$\frac{1-\nu_0}{2} < n_S < \frac{2}{1-\nu_0}. \tag{9}$$

Since $\nu_0 = C_{12}^{(0)}/C_{11}^{(0)} = -s_{12}^{(0)}/s_{11}^{(0)}$, Equation (9) gives the exact admissible parameter windows for our three backgrounds: $0.200 < n_S < 5.000$ for $\nu_0 = 0.60$, $0.335 < n_S < 2.985$ for $\nu_0 = 0.33$, and a much narrower corridor $0.900 < n_S < 1.111$ for the auxetic medium ($\nu_0 = -0.80$). Thus, moderate values such as $n_S = 0.8$ or 1.2 violate positive definiteness in the auxetic medium, whereas any value inside $n_S \in (0.900, 1.111)$ defines a thermodynamically valid material.

Within the stability window of Equation (9), we prove an **all-order neutrality theorem** using both symbolic algebra (Methods 3) and exact rational arithmetic. Its structure depends cleanly on three factors: the harmonic

order n, the distinction between subspace invariance and radial-exponent invariance, and whether the ring encloses an intact core or a void:

1. **Harmonics $n \geq 2$:** For every integer $n \geq 2$, the 4×4 cylindrical system matrix $\boldsymbol{N}_n^{(m)}$ of the matched ring (Equation 8) leaves *both* the 2D regular background eigenspace $\mathcal{V}_+(n) = \ker(\boldsymbol{N}_n^{(0)} - (n+1)\boldsymbol{I}) \oplus \ker(\boldsymbol{N}_n^{(0)} - (n-1)\boldsymbol{I})$ and the 2D decaying background eigenspace $\mathcal{V}_-(n) = \ker(\boldsymbol{N}_n^{(0)} + (n+1)\boldsymbol{I}) \oplus \ker(\boldsymbol{N}_n^{(0)} + (n-1)\boldsymbol{I})$ **identically invariant**:

$$\boldsymbol{N}_n^{(m)}\boldsymbol{Y}_\pm(n) = \boldsymbol{Y}_\pm(n)\,\boldsymbol{\Lambda}_\pm(n), \quad \mathrm{eig}(\boldsymbol{\Lambda}_\pm(n)) = \pm\left(n\,n_S \pm \sqrt{n^2 n_S^2 - n^2 + 1}\right). \tag{10}$$

Exact rational-arithmetic tests across all admissible parameter pairs give **0/504 failures** across 4 backgrounds and 14 harmonic orders up to $n = 101$ (with 6 non-positive-definite pairs excluded by Equation 9). Moreover, symbolic algebra proves that $\boldsymbol{N}_n^{(m)}\boldsymbol{Y}_\pm(n) - \boldsymbol{Y}_\pm(n)\boldsymbol{\Lambda}_\pm(n) \equiv \boldsymbol{0}$ vanishes identically for arbitrary $n \geq 2$ (with $\det\boldsymbol{Y}_{\pm,1:2} = \pm 2(K_0 + 2\mu_0) \neq 0$). Importantly, subspace invariance does *not* imply that the internal radial propagation exponents remain equal to the background values $\pm(n \pm 1)$ when $n_S \neq 1$. Instead, within $\mathcal{V}_\pm(n)$, the internal exponents $\mathrm{eig}(\boldsymbol{\Lambda}_\pm(n))$ form a complex-conjugate pair when $(1 - \nu_0)/2 < n_S < \sqrt{1 - 1/n^2}$, and become distinct real pairs when $n_S > \sqrt{1 - 1/n^2}$.

2. **Low harmonics $n = 0$ and $n = 1$:** Explicit rational checks (detailed in Supplementary Note 2) confirm that the regular 2D subspaces remain strictly invariant (**0/18** failures each): $\mathcal{V}_+(0)$ spans axisymmetric uniform pressure (r^{+1}) and rigid-body rotation ($u_\theta = r$), while $\mathcal{V}_+(1)$ spans rigid translation and the $p = +2$ biharmonic mode. In contrast, the decaying subspaces are **not invariant** whenever $n_S \neq 1$ (**18/18** non-invariant cases each). Specifically, this applies to the decaying axisymmetric hole-expansion and torque subspace $\mathcal{V}_-(0)$ (r^{-1}) as well as the $n = 1$ net-force Kelvinlet generalized subspace $\mathcal{V}_-(1)$, which exhibits logarithmic radial growth ($\boldsymbol{v}_{\mathrm{kel}} + \ln r\,\boldsymbol{v}_{\mathrm{tr}}$). Hence, Equation (8) preserves all intact-plate regular responses for $n \geq 0$, while low-order decaying multipoles at $n = 0{,}1$ remain sensitive to n_S.

3. **Intact-background neutrality vs. wrapping a traction-free void (140-digit verification):** This theorem cleanly distinguishes a neutral ring embedded in an intact medium from one wrapped around a void. (i) When a matched polar-orthotropic ring (Equation 8) of *arbitrary radial thickness* is embedded in an *intact* isotropic background, regular-subspace invariance guarantees **zero exterior scattering at every harmonic order** $n \geq 0$ ($\|\boldsymbol{S}_m(n)\| = 0$ in exact arithmetic and $< 10^{-14}$ in double precision). Nevertheless, when $n_S \neq 1$, the internal displacement and stress fields inside $a_0 \leq r \leq b$ still differ from those of the uniform plate.

(ii) When the same ring instead surrounds a *traction-free inner void* $r < a_0$ (Fig. 1b), it does **not** eliminate the inner void's scattered field, nor does it preserve the bare hole's $\sim n^4(a_0/b)^{4n-4}$ decay rate across a thick annulus. Rather, invariance of $\mathcal{V}_\pm(n)$ eliminates reflection at the outer interface ($h_\infty = 0$), while transmitting the void's field inward and outward with modified ring exponents $\mathrm{eig}(\boldsymbol{\Lambda}_\pm(n))$. Because standard IEEE-754 double precision (float64) reaches a numerical floor near 10^{-29} by $n \geq 32\text{–}64$, we verified this behavior on the $\nu_0 = 0.60$ background ($n_S = 1.2$; normalized to $C_{11}^{(0)} = 1$: $C_{rr} = C_{\theta\theta} = 1.0526$, $C_{r\theta} = 0.5474$, $G_{r\theta} = 0.1600$) using 140-digit arbitrary-precision arithmetic (Fig. 1b). While the bare hole decays to 3.90×10^{-28} ($n = 32$), 1.26×10^{-60} ($n = 64$), and 8.18×10^{-127} ($n = 128$), replacing only the outermost 1.25mm cloak layer (53.75–55mm) tracks the bare hole closely (5.07×10^{-29}, 1.23×10^{-60}, 1.45×10^{-125}). Spanning the entire 30–55mm annulus produces a slower

exponential decay governed by $p_{-}(n) \approx 0.5367n$ (6.80×10^{-18}, 5.45×10^{-36}, 3.66×10^{-72}), which still converges cleanly to $h_{\infty} = 0$. Unlike classical coated neutral inclusions [24, 25, 27, 28]—which cancel only uniform hydrostatic or shear fields ($n = 0,2$)—and unlike pre-stressed hyperelastic transformation cloaks [29], Equations (8)–(10) provide an explicit, un-prestressed linear-elastic ring family with exact subspace invariance for all $n \geq 2$.

3. Zero-parameter continuum and angularly coupled theory predicts FE performance across radial scales

We next test whether our per-order transfer theory can quantitatively predict independent T6 finite-element benchmarks without any fitted parameters. We compare the 1D axisymmetric continuum theory—using the angle-averaged stiffness $\overline{a}_i = \langle a_{i,j} \rangle_{\theta}$ of each layer—against T6 FE results across four radial near-field load classes: wide rings (55–65mm, half-width $w = 5$mm), offset rings (58–68mm, 3mm gap), half-width rings (55–60mm, $w = 2.5$mm), and a radial scan of 31 thin rings ($w = 0.3125$mm, $r_c \in [55.3125, 64.6875]$mm; Fig. 2a and Table 2). We evaluate three cloak classes optimized over 20×192 radial–angular sectors ($a \in [0.02,4.0]$, Methods 5): a 6-load boundary-trained cloak (Trained-6), boundary-repaired cloaks constrained over $\mathcal{L}_{\mathrm{BD}}$ (BC-cloak), and jointly constrained cloaks trained on both boundary loads and the 55–65mm ring (Joint-cloak) at tolerances $\tau_d \in \{10^{-3}, 10^{-4}\}$.

In the auxetic medium ($\nu_0 = -0.80$), the optimized cloaks are nearly axisymmetric, with small outer-layer angular stiffness variations ($\sigma_{\theta}(a) = 0.002–0.041$). Consequently, the zero-parameter 1D theory agrees closely with T6 FE across all 31 thin-ring positions (0.73–1.15 ×) and across the 55–65mm, 55–60mm, and nested radial spaces (0.91–1.15 ×) for both BC-cloak and Joint-cloak designs. It also accurately predicts the dominant polar harmonic order n^* at the innermost thin ring $r_c = 55.31$mm under polar harmonic projection (35 vs. 34 for Joint-cloak $\tau_d = 10^{-3}$, an exact 13 vs. 13 match at $\tau_d = 10^{-4}$, 38 vs. 39 for BC-cloak $\tau_d = 10^{-4}$, and an exact 5 vs. 5 match for BC-cloak $\tau_d = 10^{-3}$; Table 2 and Fig. 2a). Similarly, for the nearly axisymmetric Trained-6 cloak, 1D theory matches FE within 0.97–1.00× on both $\nu_0 = 0.60$ and $\nu_0 = 0.33$ (for instance, on the 55–65mm ring for $\nu_0 = 0.60$: 7.71×10^{-1} vs. 7.97×10^{-1}, with $n^* = 20|19$).

For $\nu_0 = 0.60$ and $\nu_0 = 0.33$, however, the square outer boundary induces strong 4-fold and higher-order azimuthal stiffness modulation in both BC-cloak and Joint-cloak designs. For example, the $\nu_0 = 0.60$ BC-cloak at $\tau_d = 10^{-3}$ reaches $\sigma_{\theta}(a)$ up to 0.309 in the outer layer, with individual sector stiffnesses spanning the full bounds $a \in [0.02,4.0]$ (Supplementary Fig. S1). Because this azimuthal modulation couples different angular harmonics through Toeplitz convolutions of $a(\theta)$ and $a(\theta)^{-1}$, the 1D angle-averaged model misses two opposing physical effects:

1. **Upward harmonic scattering (under-prediction by 1D averaging):** For the $\nu_0 = 0.60$ BC-cloak ($\tau_d = 10^{-3}$), azimuthal stiffness variations in the outer layer scatter smooth near-field loads into high harmonics ($n^* = 23–45$). As a result, the FE deterioration on the innermost thin ring (3.81×10^{-1}) exceeds the 1D angle-averaged prediction at $n^* = 1$ (3.57×10^{-2}) by a factor of 10.7 × (theory/FE = 0.094 ×).
2. **Phase cancellation of low-order residuals (over-prediction by 1D averaging):** Conversely, for the $\nu_0 = 0.60$ Joint-cloak designs ($\tau_d = 10^{-3}$ and 10^{-4}), the 192-sector optimizer tunes the azimuthal Fourier phases to partially cancel low-order residuals that remain in the 1D mean profile. Consequently, the 1D mean over-predicts FE deterioration across the four radial benchmark classes by 5.8–19.0 × at $\tau_d = 10^{-3}$ (13.2 × on the 55–65mm ring, and up to 22.9 × across the 31-ring scan) and by 6.5–83.2 × at $\tau_d =$

10^{-4} (51.4× on 55–65mm, 83.2× on the 58–68mm offset ring, and up to 93.4 × on the outer steps of the 31-ring scan).

Once we include exact angular Toeplitz coupling over $|k| \le K_c = 80$—forming 644×644 layer state matrices and 322×322 impedance blocks with zero fitted parameters (Fig. 2b)—these discrepancies vanish in the high-n^* regime. Across all 27 high-n^* benchmark points spanning all three backgrounds, the coupled theory agrees with T6 FE within $0.974–1.028\times$ (0.97–1.03×, blue circles in Fig. 2b). In the remaining 15 low-n^* cases (teal squares in Fig. 2b: 14 cases with $n^* \le 9$, plus the offset ring at $n^* = 14$ for the $\nu_0 = 0.60$ $\tau_d = 10^{-4}$ Joint-cloak), the circular-plate theory ($R_{\mathrm{out}} = 75\mathrm{mm}$) and square-plate T6 FE ($L = 75\mathrm{mm}$) differ systematically by $0.821–2.147\times$ (0.82–2.15×). This offset reflects the sensitivity of low angular harmonics to the circular-versus-square outer plate geometry.

4. High-resolution T6 finite-element verification of thin-source saturation and convergence

To determine whether near-field deterioration diverges or saturates as radial loads become narrower than $0.3125\mathrm{mm}$ and angular cutoffs exceed $K = 64$, we compared our a priori analytical predictions against an independent fine T6 FE mesh (**567,938 DOFs**, 283,104 quadratic elements, and 2,304 boundary trace DOFs on $r = 55\mathrm{mm}$). We evaluated both thin ($w = 0.3125\mathrm{mm}$) and ultrathin ($w = 0.15625\mathrm{mm}$) boundary-contact rings at angular cutoffs $K \in \{64,96,128\}$. Across all 30 benchmark combinations covering five auxetic designs—BC-cloak ($\tau_d = 10^{-4}$), Joint-cloak ($\tau_d = 10^{-3}$ and 10^{-4}), and two bounded-stiffness designs with $a \in [0.71,2.45]$ (Nominal-bounded and Robust-bounded)—the 567,938-DOF FE results match our zero-parameter theory within $0.995–1.026\times$ across every cutoff and width (Fig. 2c, Table 3, and Supplementary Table S1):

- **Saturation with angular cutoff:** Increasing K from 64 to 128 yields only bounded growth across all 10 fixed-width pairs—ranging from $1.000002\times$ (Joint-cloak $\tau_d = 10^{-4}$, $a_{20} = 1.001$) to $1.090\times$ ($1.0898\times$ on Nominal-bounded at $w = 0.15625\mathrm{mm}$, where deterioration moves from $2.05\tau \to 2.23\tau$)—confirming high-K saturation.
- **Controlled thinning growth and bounded-stiffness acceptance:** Halving the radial source width from $0.3125\mathrm{mm}$ to $0.15625\mathrm{mm}$ at $K = 128$ increases deterioration by modest factors of $1.056–1.287\times$ (1.056×, 1.165×, 1.177×, 1.203×, and 1.287×), closely matching the theoretical range (1.06–1.27×). Notably, on the nominal circular void under the ultrathin $K = 128$ load, the geometry-tolerant Robust-bounded cloak achieves 0.977τ (0.9768τ with 6-point quadrature and 0.9757τ with 150-point quadrature, compared with the predicted 0.973τ), staying 2.32% below the tolerance τ on this geometry.

Mesh- and quadrature-convergence audits (Supplementary Note 3, Supplementary Fig. S2, and Supplementary Tables S2a–b) verify the numerical reliability of these benchmarks. On the 567,938-DOF mesh, discretization sensitivity drops to $\le 0.11\%$ for Robust-bounded (0.107% cross-mesh difference relative to a 350,978-DOF radially refined mesh, and $0.089\%–0.108\%$ between 6-point and 150-point quadrature) and to $\le 0.02\%$ for buffered designs. Extreme-contrast unbuffered designs retain $\le 1.11\%$ quadrature sensitivity and $1.10\%–4.88\%$ cross-mesh sensitivity on the fine mesh, whereas a coarser 252,674-DOF mesh suffers $+16.61\%–45.80\%$ discretization and quadrature aliasing under ultrathin $K = 128$ loads. Finally, polar angle-weighted harmonic extraction on the 567,938-DOF mesh (Methods 6) shows that unbuffered cloaks concentrate thin-source scattering near the harmonic cutoff ($n^* = 121–127$), whereas outer-edge buffering shifts the dominant response down to low polar orders ($n^* = 2,6$; Supplementary Table S1).

5. Outer-edge matching without near-field training, Pareto trade-offs, and finite-arc local patch tests

Equation (5) immediately suggests a practical design principle: matching the outer layers of a cloak to the background impedance ($e_1 = e_2 = 0$, $h_\infty = 0$) should eliminate the high-order asymptotic floor even when the cloak is optimized using **boundary loads alone**. To evaluate this strategy rigorously, however, we must distinguish three different limits:

1. the fixed-order limit $\lim_{d,w\to 0^+} h_n(d,w)$ at a given harmonic n;
2. the high-order pressed-source floor $h_\infty = \lim_{n\to\infty}\lim_{r_c\to b^+} h_n(r_c)$ of Equation (6); and
3. the all-order worst-case thin-source limit $\lim_{w\to 0^+}\sup_n h_n(d,w)$.

Because Equations (5)–(6) govern only the $n \to \infty$ asymptote, eliminating the high-order floor ($h_\infty = 0$) **does not guarantee** $\max_n h_n = 0$ **or** $\max_n h_n \le \tau$. Low and intermediate angular harmonics ($n \lesssim b/w_{\mathrm{buf}}$) can still penetrate the outer buffer, sense the buried inner stiffness mismatch, and dominate the worst-case deterioration h.

To test this prediction, map the trade-off between shielding and non-deterioration, and quantify residual low- and intermediate-order errors, we solved the axisymmetric 20-layer circular-plate optimization problem (Fig. 3a,b and Table 4; see Supplementary Note 4 for normalization and circular-versus-square domain scaling). We examined four optimization regimes—unconstrained boundary optimization, intermediate Pareto constraints ($h_{\mathrm{BD}} \le 50\tau, 10\tau$), strict boundary-only repair ($h_{\mathrm{BD}} \le 0.70\tau$, $n \le 12$), and joint boundary plus 55– 65mm ring repair—while fixing the outermost $n_{\mathrm{fix}} \in \{0,1,2,4,6\}$ layers (buffer thickness $w_{\mathrm{buf}} = 1.25 n_{\mathrm{fix}}$mm) to the background stiffness $a = 1$:

- **Shielding-versus-non-deterioration Pareto trade-off and strong-shielding buffers:** When evaluated over the *full* circular boundary space $\mathcal{L}_{\mathrm{BD}}$ ($n \le 12$), the unconstrained Trained cloak on $\nu_0 = 0.60$ lowers the worst-case total error to $E_{\max,C} = 0.305$ by strongly shielding the high-visibility $n = 0$ and $n = 2$ modes ($E_0 = 0.152$, $E_2 = 0.305$). However, scalar isotropic stiffening simultaneously amplifies low-visibility higher harmonics ($E_5 = 0.175$ vs. bare-hole 0.0079; $E_6 = 0.170$ vs. 0.0008), causing severe boundary deterioration ($h_{\mathrm{BD}} = 169.0\tau$, or 168.95τ). Enforcing strict non-deterioration across *every* boundary harmonic ($h_n \le 0.70\tau$ for all $n \le 12$) activates constraints at $n = 1,2,5,6$ and limits isotropic worst-case shielding to $E_{\max,C} = 0.864$, although strong shielding is still retained under specific symmetric loads such as equibiaxial tension (for example,$R_{\mathrm{biax}} = 0.273$ for the square-plate $\nu_0 = 0.60$ Joint-cloak in Table 5).

Crucially, removing the high-order reflection floor with a 2.5mm outer buffer **does not require giving up strong boundary shielding**. Adding a 2.5mm buffer to the unconstrained strong-shielding cloak preserves $E_{\max,C} = 0.345$ (a 65.5% reduction in worst-case error) while eliminating the pressed-source floor ($h_\infty \to 0\tau$), reducing thin-contact deterioration ($1306.8\tau \to 701.4\tau$), and suppressing compact $\Delta\theta = 2^\circ$ contact-patch error by $10.4\times$ ($105.9\tau \to 10.2\tau$; with a $w_{\mathrm{buf}} = 5.0$mm buffer, this drops by $286\times$ to 0.37τ; Table 4 and Supplementary Note 5). Likewise, along the Pareto curve, relaxing the boundary tolerance to $h_{\mathrm{BD}} \le 50\tau$ (or 10τ) with a 2.5mm buffer maintains strong shielding at $E_{\max,C} = 0.390$ (or 0.573), collapses h_∞ from 781.1τ (or 80.9τ) to 0τ, and slashes $\Delta\theta = 2^\circ$ contact-patch error by $275\times$ ($393.2\tau \to 1.43\tau$) and $558\times$ ($44.6\tau \to 0.08\tau$), respectively.

- **Collapse of h_∞ under strict boundary repair ($\nu_0 = 0.60, \tau = 10^{-3}$):** Without a buffer ($w_{\mathrm{buf}} = 0\mathrm{mm}$), strict boundary repair leaves an outer-layer mismatch of $a_{20} = 0.652$, which creates a large pressed-source floor ($h_\infty = 270.0\tau$), thin-contact ($w = 0.3125\mathrm{mm}$) deterioration of 137.8τ ($n^* = 64$), and $55-65\mathrm{mm}$ ring deterioration of 13.83τ ($n^* = 29$). Fixing just one outer layer ($1.25\mathrm{mm}$ buffer, $a_{20} = 1$) drives $h_\infty = 0\tau$, cuts thin-contact deterioration by $13.3\times$ to 10.39τ ($n^* = 52$), and reduces $55-65\mathrm{mm}$ deterioration to 2.54τ ($n^* = 6$). Fixing two outer layers ($2.50\mathrm{mm}$ buffer, $a_{19} = a_{20} = 1$)—using **zero near-field training loads**—lowers circular-plate thin-contact deterioration to 2.85τ ($n^* = 6$) and $55-65\mathrm{mm}$ deterioration to 1.78τ, with virtually no loss in boundary shielding ($E_{\max,C} = 0.867$, only +0.003 above 0.864). Further widening the buffer to $w_{\mathrm{buf}} = 5.0-7.5\mathrm{mm}$ causes the error to saturate near 2.46τ (Fig. 3b). Combining the $2.50\mathrm{mm}$ buffer with $55-65\mathrm{mm}$ joint constraints lowers circular-plate thin-contact error further to 1.22τ ($n^* = 2$, $E_{\max,C} = 0.879$).
- **Residual low-order errors on buffered boundary designs:** Across other backgrounds and stricter tolerances (Table 4), eliminating $h_\infty = 0$ by boundary-only buffering still leaves low-order residuals above τ. Specifically, $\nu_0 = 0.33$ ($\tau = 10^{-3}$) retains 2.02τ ($n^* = 6$), and $\nu_0 = -0.80$ ($\tau = 10^{-3}$) retains 5.52τ ($n^* = 5$). At the tighter tolerance $\tau = 10^{-4}$, boundary repair plus a $2.5\mathrm{mm}$ buffer on $\nu_0 = -0.80$ leaves 8.13τ ($n^* = 6$, compared with 73.98τ unbuffered), while joint repair plus a $2.5\mathrm{mm}$ buffer leaves 2.29τ ($n^* = 12$). These residual errors directly confirm that setting $h_\infty = 0$ shuts down the high-n flat-interface reflection channel without altering the inner-cloak low- and mid-n physics.

We next tested these four $\nu_0 = 0.60$ designs—Unbuffered BC-cloak, Buffered BC-cloak ($w_{\mathrm{buf}} = 2.5\mathrm{mm}$), Unbuffered Joint-cloak, and Buffered Joint-cloak ($w_{\mathrm{buf}} = 2.5\mathrm{mm}$)—on the independent 567,938-DOF T6 square-plate mesh. Every theoretical prediction is confirmed (Fig. 3c and Table 3):

- **Zero-parameter high-order agreement and low-order geometry effects:** For both unbuffered designs (polar $n^* = 48-127$), all 12 thin-source T6 FE values agree with circular-plate theory within $0.997-1.004\times$ (1.00×). For the buffered designs, where the high-n floor disappears and low-order hole modes govern the peak, T6 FE matches the exact dominant polar harmonic (Buffered BC-cloak: $n^* = 6$, FE $3.05-3.09\tau$ vs. circular theory $2.834-2.878\tau$, ratio 1.075–1.076×; Buffered Joint-cloak: $n^* = 2$, FE $1.63-1.65\tau$ vs. circular theory $1.211-1.234\tau$, ratio 1.341–1.342×). These small constant factors arise from the circular-versus-square outer plate geometry at low n^*.
- $48.6\times$ **near-field error reduction without near-field training:** Adding the $2.5\mathrm{mm}$ buffer to boundary-only repair reduces thin-contact ($w = 0.3125\mathrm{mm}$, $K = 128$) deterioration from 148.0τ to 3.05τ—a $48.6\times$ **reduction** (48.56×) achieved *without any near-field training loads*. It also makes the response insensitive to the angular cutoff $K \in \{64,96,128\}$ and to both hat widths: the total max/min variation is only $1.015\times$ ($3.05\tau \to 3.09\tau$) for the Buffered BC-cloak and $1.018\times$ ($1.63\tau \to 1.65\tau$) for the Buffered Joint-cloak. Across all six thin-source classes, the designs maintain the strict ranking Unbuffered BC > Unbuffered Joint > Buffered BC > Buffered Joint.

Spatially localized finite-arc force patches on unbuffered and buffered BC-cloaks (Fig. 4 and Supplementary Table S3). Spectral ring classes localize forces radially, but they still optimize worst-case Fourier superpositions across $k \le K$. To test a more physically realistic loading scenario, we evaluated how strongly high-order reflections are excited by a single **spatially localized, self-equilibrated force patch** of definite arc length $2b\,\Delta\theta$ and radial clearance $d = r_{\min} - b \ge 0$, without re-optimizing either cloak. We applied radial body-force patches $\boldsymbol{f}(r,\theta) = \psi(r; b+d+w, w)\,[b_0(\theta) - c\,b_2(\theta)]\boldsymbol{e}_r$ supported strictly within

$|\theta| \le \Delta\theta$ and $r \in [b+d, b+d+2w]$, where $b_0(\theta) = \cos^2(\pi\theta/(2\Delta\theta))$ and $b_2(\theta) = (\theta/\Delta\theta)^2 b_0(\theta)$. The constant c is calibrated so that the net force and net moment vanish on the 150-point T6 quadrature mesh to relative residual $< 10^{-13}$ (Fig. 4a). Direct evaluation on the 567,938-DOF mesh reveals three clear trends:

1. **Angular footprint sweep at interface contact ($d = 0$, $w = 0.3125$mm, Fig. 4b):** We progressively narrowed the contact patch from $\Delta\theta = 30^\circ$ (57.6mm arc, spectral peak $n_{\text{peak}} = 9$) through 15° (28.8mm, $n_{\text{peak}} = 17$), 8° (15.4mm, $n_{\text{peak}} = 32$), and 4° (7.7mm, $n_{\text{peak}} = 64$) down to 2° (3.8mm, $n_{\text{peak}} = 127$). Because local self-equilibration suppresses the $n = 1$ force mode, the bare-hole error energy E_V decreases monotonically from 13.61τ to 0.912τ (15°), 0.076τ (8°), 0.005τ (4°), and 0.0003τ (2°). The unbuffered BC-cloak exhibits the opposite behavior, rising sharply above τ: from 13.06τ ($h = -0.544\tau$ at 30°) to 5.11τ (15°, $h = +4.19\tau$), 24.73τ (8°, $n^* = 33$), 81.06τ (4°, $n^* = 59$), and 130.83τ (2°, $n^* = 98$). At the thinner width $w = 0.15625$mm, it reaches 150.66τ ($n^* = 104$)—already 83% of the unconstrained spectral ceiling 182.4τ.

In sharp contrast, the boundary-trained $+2.5$mm Buffered BC-cloak suppresses both total error and incremental deterioration across every compact patch: 0.911τ (15°, $h = -0.001\tau$), 0.168τ (8°, $h = 0.092\tau$), 0.058τ (4°, $h = 0.053\tau$—a $1{,}520\times$ drop in h and a $1{,}400\times$ drop in absolute error E), and 0.008–0.009τ at 2°.

2. **Stand-off clearance sweep ($\Delta\theta = 4^\circ$, $w = 0.3125$mm, $d \in [0,8]$mm, Fig. 4c):** Moving the fixed 7.7mm self-equilibrated patch radially away from $r = 55$mm activates the exponential background filter $(b/r)^{n-1}$. As a result, the unbuffered reflection energy drops smoothly from 81.06τ ($d = 0$, $n^* = 59$) through 76.14τ (0.25mm), 65.61τ (0.5mm), 42.85τ (1.0mm), 15.64τ (2.0mm, $n^* = 40$), and 2.37τ (4.0mm, $n^* = 30$) down to 0.142τ (8.0mm, $n^* = 20$). Meanwhile, the buffered cloak remains $\le 0.058\tau$ at every stand-off distance. Across all 12 intermediate and compact patch cases ($\Delta\theta \le 15^\circ$, $d = 0$–8mm), zero-parameter continuum theory using exact regular eigenvector propagation agrees with the full square-plate 567,938-DOF T6 FE results within **0.990–1.005×** (Supplementary Table S3).

3. **Real-space exterior displacement error maps ($\Delta\theta = 4^\circ$, $d = 0$, Fig. 4d):** Plotting the 2D displacement error field $|\boldsymbol{u} - \boldsymbol{u}_0|/\sqrt{\mathcal{E}_0}$ outside $r = 55$mm directly visualizes the reflection mechanism. The unbuffered cloak radiates intense, short-wavelength, multi-lobe ripples along the interface (peaking at 7.6×10^{-2}, which is $184\times$ larger than the bare-hole peak of 4.1×10^{-4}). Adding the 2.5mm buffer suppresses this peak exterior distortion by $30\times$, down to 2.5×10^{-3}.

Beyond a simple step buffer, two alternative outer-edge designs trained on boundary loads alone confirm the same interface-continuity principle (Fig. 3a,b and Table 4):

1. **Smooth cosine-tapered edge:** Using a 4-layer cosine taper over 50–55mm eliminates the reflection floor ($h_\infty = 0\tau$) and lowers 55–65mm ring deterioration to 1.65τ and thin-contact ($w = 0.3125$mm) deterioration to 2.55τ on $\nu_0 = 0.60$ (and to 1.26τ and 1.95τ, respectively, on $\nu_0 = 0.33$), while maintaining $E_{\max,C} = 0.867$.

2. **Hybrid scalar + Suo-matched polar-orthotropic outer shell:** Replacing the outermost 2 layers (52.5–55mm) with a compliance-matched polar-orthotropic shell ($n_S = 1.2$, Equation 8) reduces circular-plate thin-contact deterioration to 2.61τ on $\nu_0 = 0.60$ (and 1.79τ on $\nu_0 = 0.33$). At the same time, it improves the worst-case boundary error to $E_{\max,C} = 0.857$ (and 0.850 on $\nu_0 = 0.33$), outperforming

unbuffered scalar boundary repair (0.864,0.860). This advantage arises because the matched orthotropic shell actively assists low-order shielding while introducing zero high-order reflection floor.

6. Constructive geometry-tolerant bounded-stiffness design and physical benchmarks

Practical metamaterial fabrication often precludes extreme stiffness ratios ($a \in [0.02,4.0]$) and perfectly circular voids. To assess manufacturability under realistic constraints, we performed joint boundary–near-field optimization within a modest stiffness range $a \in [0.71,2.45]$ ($3.45\times$ maximum contrast) in the auxetic medium ($\nu_0 = -0.80$, $\tau = 10^{-3}$). We optimized simultaneously across four hole geometries: the nominal circle ($a_0 = 30\text{mm}$), a $+1.25\text{mm}$ enlarged hole, a -1.5mm shrunk hole, and a 1.5mm x-eccentric hole (Fig. 5a and Table 5).

When bounded-stiffness optimization is constrained only on the nominal circle (Nominal-bounded), the resulting cloak passes boundary-displacement tests across all four shapes ($0.204–0.578\tau$), yet fails on perturbed geometries under exterior body forces and near-field loads. Specifically, on the shrunk hole, deterioration exceeds tolerance for smooth polynomial body forces ($\mathcal{L}_{\mathrm{BF}}$: 1.219τ), the wide ring (1.647τ), and the half-width ring (2.172τ); on the eccentric hole, the half-width ring also fails (1.284τ). In contrast, our multi-geometry robust design (Robust-bounded)—jointly constrained on boundary displacements and the $55–65\text{mm}$ ring across all four shapes—passes independent T6 FE verification across **all four geometries** for every tested load family, and also passes the ultrathin $K = 128$ test on the nominal circle:

- Boundary displacement ($\mathcal{L}_{\mathrm{BD}}$): $h \in [0.174, 0.549]\tau \le \tau$ across all 4 geometries;
- Smooth polynomial exterior body forces ($\mathcal{L}_{\mathrm{BF}}$, total degree ≤ 6 on Ω_{obs} with clamped outer edges; Methods 5): $h \in [0.066, 0.448]\tau \le \tau$ across all 4 geometries;
- Wide near-field ring ($55–65\text{mm}$): $h \in [0.157, 0.601]\tau \le \tau$ across all 4 geometries;
- Unconstrained closer near-field ring ($55–60\text{mm}$): $h \in [0.238, 0.792]\tau \le \tau$ across all 4 geometries;
- Ultrathin $w = 0.15625\text{mm}$, $K = 128$ contact ring (nominal circle): $h = 0.9768\tau$ (6-point quadrature) and 0.9757τ (150-point quadrature).

Separating the two cost baselines shows that geometry tolerance is remarkably inexpensive. Within the same bounded stiffness window $[0.71,2.45]$, adding 4-geometry robustness increases the nominal worst-case boundary error energy ratio by only $+1.03\%$ ($E_{\max,C} = 0.9047$ vs. 0.8955; T6 FE: 0.8816 vs. 0.8747). Even relative to the wide-bound [0.02,4.0] Joint-cloak ($\tau_d = 10^{-3}$, $E_{\max,C} = 0.8537$), the combined penalty of tightening the stiffness contrast by $58\times$ and enforcing 4-shape robustness is only $+5.97\%$ (0.9047 / 0.8537).

To evaluate practical cloaking performance under canonical deformations, we conducted physical boundary-value and perturbation benchmarks (Fig. 5b and Table 5). Here, we report paired cloak-to-bare-void exterior error-energy ratios under affine boundary displacements corresponding to equibiaxial tension (R_{biax}), x-axis uniaxial tension (R_{ux}), and pure shear (R_{shear}):

1. **Canonical boundary loads:** The $\nu_0 = 0.60$ Joint-cloak ($\tau_d = 10^{-3}$) reduces exterior error energy relative to the bare hole to $R_{\mathrm{biax}} = 0.273$ (displacement-error norm ratio 0.523), $R_{\mathrm{ux}} = 0.316$, and $R_{\mathrm{shear}} = 0.750$. In the auxetic medium, the Joint-cloak ($\tau_d = 10^{-3}$) achieves $R_{\mathrm{biax}} = 0.525$ (norm 0.725), $R_{\mathrm{ux}} = 0.841$, and $R_{\mathrm{shear}} = 0.828$, while Robust-bounded achieves $R_{\mathrm{biax}} = 0.657$ (norm 0.810), $R_{\mathrm{ux}} = 0.886$, and $R_{\mathrm{shear}} = 0.879$.

2. **Multi-load boundary suite and engineering observables:** Across 8 physical affine boundary loads in the auxetic medium (Methods 5), the $\tau_d = 10^{-3}$ Joint-cloak keeps exterior error energy strictly below the bare hole in all 8 cases ($\mathrm{ratio}_E = 0.525\text{–}0.820$). Under equibiaxial tension on the nominal circle, it reduces the clamped-boundary reaction-force deviation norm ratio to $\mathrm{ratio}_F = 0.713$ (and 0.914 at $\tau_d = 10^{-4}$) and the probe-ring strain deviation ratio to $\mathrm{ratio}_s = 0.685$ (and 0.921 at $\tau_d = 10^{-4}$). By comparison, Trained-6 amplifies exterior energy, reaction-force deviation, and probe-ring strain by $12.683\times$, $3.597\times$, and $3.674\times$, respectively.
3. **Material and geometric perturbations:** The auxetic $\tau_d = 10^{-3}$ Joint-cloak stays below the bare-hole error across all 32/32 $\pm 5\%$ background modulus shifts ($\mathrm{ratio}_E \leq 0.844$), all 20/20 realizations of 5% random layer-stiffness noise (0.496–0.609), all 20/20 realizations of 10% noise (0.484–0.706), and all 3/3 perturbed hole shapes (enlarged: 0.908; shrunk: 0.499; eccentric: 0.687). By contrast, the tighter $\tau_d = 10^{-4}$ Joint-cloak loses equibiaxial shielding under $+1.25\mathrm{mm}$ hole enlargement ($\mathrm{ratio}_E = 1.292$). Across all 256 perturbation realizations, the reaction-force and probe-strain ratios agree with the direction of the energy ratio in 91.4% (234/256) and 98.8% (253/256) of cases (see Supplementary Table S4 for a unified summary of design families and scope boundaries).

7. Outer-edge mismatch and discrete-beam verification in lattice cloaks

To verify that outer-edge impedance mismatch also governs discrete structural metamaterials—such as the aperiodic and disordered lattice cloaks studied by Wang et al. [15] and Yang et al. [17]—we analyzed three self-constructed square-lattice cloaks: a 4-load lattice, a 100-load lattice, and a uniform lattice ring. Their strut geometries were extracted from 1500×1500-pixel maps with lattice pitch $\ell = 4.839\mathrm{mm}$, background strut width $b_0 = 0.938\mathrm{mm}$, and effective shear anisotropy $\kappa_{\mathrm{lat}} = 2\ell^2/b_0^2 = 53.2$ (Fig. 5c and Supplementary Fig. S3).

Direct measurement of all 564 cloak struts in $30\text{–}55\mathrm{mm}$ reveals severe outer-edge width discontinuities left behind by boundary-only training. In the $45\text{–}50\mathrm{mm}$ annulus, $96.4\%\text{–}100\%$ of struts deviate from b_0 by more than $\pm 10\%$: specifically, 61.4% of struts in the 4-load lattice, 87.1% in the 100-load lattice, and 100% in the uniform ring exceed $1.5b_0$ (with median widths of $1.84b_0, 2.03b_0, 1.65b_0$, respectively). Even in the outermost $50\text{–}55\mathrm{mm}$ shell straddling $r = b$, $27.3\%\text{–}33.3\%$ of members still exceed $1.5b_0$ (Supplementary Fig. S3b).

Going beyond homogenized Q4 continuum estimates (where the error ratio jumps from 8.9–16.7× on boundary loads → 68.0–311.7× in the near field), we performed direct **2D discrete beam finite-element verification** across all 961 grid nodes (2,883 DOFs $[u_x, u_y, \theta_z]$ and 1,628 active struts; Methods 5 and Supplementary Table S5). To capture thick-strut shear deformation ($b/\ell \approx 0.19\text{–}0.41$) alongside bending, we modeled every strut with both **Timoshenko beam elements** ($k_s = 5/6, \nu_s = 0.33$) and slender **Euler–Bernoulli beam elements**:

1. **Discrete near-field amplification across ring and node-level loads (Fig. 5c):** In the 2D Timoshenko beam model, the cloak-to-bare-void exterior error-energy ratio on the worst-deterioration mode jumps sharply from $8.3\text{–}14.7\times$ under P_4 boundary displacements (8.9× for 4-load, 14.7× for 100-load, and 8.3× for uniform) to $87.9\text{–}113.0\times$ on $55\text{–}65\mathrm{mm}$ rings, $102.5\text{–}177.4\times$ on $61\text{–}71\mathrm{mm}$ rings, and $134.6\text{–}248.2\times$ on $65\text{–}75\mathrm{mm}$ outer rings. Under the full discrete exterior nodal-force space in $55 < r < 65\mathrm{mm}$—which captures cell-scale diffraction without Fourier truncation—the ratio similarly reaches

$88.3-117.2\times$. Euler–Bernoulli beam elements assign higher flexural stiffness to thick struts, producing even larger ratios (10.2–19.3× on boundary loads → 92.5–425.8× in the near field, bracketing the homogenized Q4 estimates from above). Both discrete models consistently confirm an approximately 10-fold jump in error amplification under near-field loading.

2. **Direct discrete outer-ring buffering (Supplementary Fig. S3c and Supplementary Table S5):** Simply resetting the outermost cloak struts in $50-55\text{mm}$ ($\sim 1\ell$) and $45-55\text{mm}$ ($\sim 2\ell$) back to the background width b_0 —without re-optimizing any inner bars—monotonically reduces discrete exterior nodal deterioration h. Across the three designs, this metric drops from $0.486 \rightarrow 0.364 \rightarrow 0.178$ (a 2.74× reduction for 100-load), $0.402 \rightarrow 0.278 \rightarrow 0.176$ (2.28× for 4-load), and $0.316 \rightarrow 0.252 \rightarrow 0.109$ (2.90× for the uniform ring), while the worst-case boundary error $E_{\max,C}$ shifts by only $+0.019-0.037$.

Discussion

Across all isotropic, polar-orthotropic, and discrete square-lattice cloaks studied here, outer-edge impedance mismatch controls the asymptotic **high-order** near-field deterioration floor. Once this floor is removed ($h_\infty = 0$), however, the overall worst-case response can still be governed by residual low- and intermediate-order hole modes. Both external-boundary validation and high-order near-field failure stem from the same spatial spectral filter: regular fields from a source at inner clearance $r_{\min}$ or far radius r_{src} decay inward as $(b/r_{\text{src}})^{n-1}$. Consequently, boundary loads ($r_{\text{src}} = R_{\text{out}}$) carry negligible weight at $n \gg 1$ and leave outer-edge stiffness jumps ($(\mu_L, K_L) \neq (\mu_0, K_0)$) unconstrained.

While bare-void scattering amplitudes decay exponentially as $\|\boldsymbol{S}_V(n)\|_2 \sim \kappa_0^{-1}(1-q^2)^2 n^2 q^{2n-2}$ (with unit-incident-energy baseline $v_n \sim \kappa_0^{-1}(1-q^2)^4 n^4 q^{4n-4}$ for $q = a_0/b$ and decay rate $4\ln q$), any mismatched isotropic outer layer creates a finite flat-interface reflection floor (e_1, e_2) and a positive pressed-source limit $h_\infty > 0$ (Equation 6). Both spectral thin-hat loads and compact, localized finite-arc patches ($2b\,\Delta\theta = 3.8-15.4\text{mm}$, reaching 150.7τ on the unbuffered boundary cloak) excite this floor directly. In contrast, our all-order polar-orthotropic subspace-invariance theorem clarifies the boundary between high-order interface neutrality and classical low-order neutral inclusions [24, 25, 27, 28]. Uniform-field neutral coatings cancel void scattering only at hydrostatic ($n = 0$) and shear ($n = 2$) orders; by contrast, compliance matching leaves both regular and decaying background subspaces invariant at *every* $n \geq 2$ around an intact core, and cancels the outer-edge floor ($h_\infty = 0$)—without removing residual inner-hole multipoles—around a traction-free void.

This spectral picture reconciles previous boundary-trained cloaks—including aperiodic, compatible-boundary, disordered, and two-stage minimax designs [15–18]—with near-field breakdown without invalidating their external-boundary performance. At the same time, it establishes two complementary design rules with clear quantitative limits:

1. **Outer-edge impedance matching without near-field training:** Enforcing a 2.5mm background buffer (or a smooth cosine taper) removes the high-order asymptotic floor ($h_\infty = 0$) using *boundary loads alone*. This cuts spectral thin-contact error by $48.6\times$ ($148.0\tau \rightarrow 3.05\tau$) and localized self-equilibrated $\Delta\theta = 4^\circ$ contact-patch error by $> 1{,}400\times$ ($81.06\tau \rightarrow 0.058\tau$). Along the Pareto frontier, buffering also preserves strong boundary shielding ($E_{\max,C} = 0.345-0.573$) while suppressing compact $\Delta\theta = 2^\circ$ patch reflections by $10.4-558\times$. Similarly, a compliance-matched polar-orthotropic outer shell (Equations 8–10) achieves $h_\infty = 0$ while improving strict boundary shielding ($E_{\max,C} = 0.857$ on $\nu_0 = 0.60$). Nevertheless, $h_\infty = 0$

does not remove residual low-order hole modes: strict all-mode non-deterioration imposes a Pareto trade-off ($E_{\max,C} = 0.864$ for isotropic rings), and buffered boundary-only designs retain low-order residuals above τ ($3.05–3.09\tau$ on $\nu_0 = 0.60$, and 8.13τ on $\nu_0 = -0.80$ at $\tau = 10^{-4}$).

2. **Joint boundary–near-field constraints with bounded stiffness:** Adding a moderate near-field ring constraint ($55–65\text{mm}$) suppresses intermediate harmonics ($n \sim 6–40$). This enables the bounded-stiffness Robust-bounded cloak ([0.71,2.45]) to pass all four hole shapes across boundary displacements, polynomial exterior body forces, $55–65\text{mm}$, and $55–60\text{mm}$ loads ($\leq 0.792\tau$), and to achieve 0.9768τ (6-point) / 0.9757τ (150-point) on the nominal circle under the ultrathin $K = 128$ source. Still, under the stricter tolerance $\tau = 10^{-4}$ in the auxetic medium, a residual of 2.29τ at $n^* = 12$ persists even with buffering.

From a manufacturing perspective, the compliance-matched polar-orthotropic shell of Equation (8) can be realized using polar-oriented cross-ply fiber laminates or symmetric radial–circumferential cellular frames aligned with (r, θ). Such architectures naturally enforce $C_{rr} = C_{\theta\theta}$ while allowing independent tuning of the shear stiffness $G_{r\theta}$ via diagonal bracing or ligament slenderness [3, 10, 12]. Equation (9) also highlights an important practical constraint on material sensitivity: conventional backgrounds ($\nu_0 = 0.33,0.60$) offer wide positive-definite stability windows ($n_S \in (0.335,2.985)$ and $(0.200,5.000)$), whereas strongly auxetic media ($\nu_0 = -0.80$) allow only a narrow corridor $n_S \in (0.900,1.111)$, demanding tighter fabrication tolerances for anisotropic realizations.

Three physical and geometric boundaries define the scope of our findings (see Methods 6 and Supplementary Note 4 for domain-size scaling, normalization sensitivity, and convergence audits). First, all continuum and discrete-lattice validations in this study are analytical and finite-element based (up to 567,938-DOF T6 and 2,883-DOF Timoshenko beam models); experimental verification on 3D-printed architected plates using digital image correlation under localized indentation remains an important direction for future work. Second, cross-specimen scaling shows that geometry-independent invariance holds quantitatively only in the high-order outer-edge regime ($1.009–1.013\times$ consistency on a fixed exterior annulus between $L = 75\text{mm}$ and 125mm plates), whereas low-order hole modes depend on outer plate size and energy normalization ($0.70–1.63\times$, consistent with the $0.82–2.15\times$ circular-versus-square offset at low n^*). Third, the 0.9768τ ultrathin-source bound on Robust-bounded applies specifically to the nominal circular void (2.32% below τ) rather than as a universal guarantee for arbitrary continuous near-field sources.

Looking beyond elastostatic plates, the underlying mechanism—exponential filtering of high spatial harmonics $(b/r_{\text{src}})^{n-1}$ by distant boundary objectives, leaving outer-interface impedance jumps unpenalized—is generic to elliptic partial differential equations, as illustrated by our exact 2D conduction analogue (Equation 7). It therefore provides a broad interface-continuity principle for inverse-designed elastic, thermal, acoustic, and electromagnetic metamaterials.

Methods

1. Per-angular-order state-space formulation and exact Riccati impedance propagation

In polar coordinates (r, θ) with logarithmic radius $s = \ln r$, combining the elastostatic equilibrium equations $\nabla \cdot \boldsymbol{\sigma} = \mathbf{0}$ with the cylindrically orthotropic constitutive relations $\sigma_{rr} = C_{rr}\varepsilon_{rr} + C_{r\theta}\varepsilon_{\theta\theta}$, $\sigma_{\theta\theta} = C_{r\theta}\varepsilon_{rr} +$

$C_{\theta\theta}\varepsilon_{\theta\theta}$, and $\sigma_{r\theta} = 2G_{r\theta}\varepsilon_{r\theta}$ for the state vector $\boldsymbol{y}_n(s) = [U_n, V_n, r\Sigma_{rr,n}, r\Sigma_{r\theta,n}]^{\mathrm{T}}$ $(n \geq 1)$ yields $\mathrm{d}\boldsymbol{y}_n/\mathrm{d}s = \boldsymbol{N}_n\boldsymbol{y}_n$, where

$$\boldsymbol{N}_n(C_{rr}, C_{\theta\theta}, C_{r\theta}, G_{r\theta}) = \begin{bmatrix} -c & -cn & C_{rr}^{-1} & 0 \\ n & 1 & 0 & G_{r\theta}^{-1} \\ E_s & nE_s & c & -n \\ nE_s & n^2E_s & nc & -1 \end{bmatrix}, \quad c = \frac{C_{r\theta}}{C_{rr}},\ E_s = C_{\theta\theta} - \frac{C_{r\theta}^2}{C_{rr}}. \tag{11}$$

Across any homogeneous layer $r \in [r_i, r_{i+1}]$ with transfer matrix $\boldsymbol{E}_i = \exp(\boldsymbol{N}_n \ln(r_{i+1}/r_i)) = \begin{bmatrix} \boldsymbol{E}_{11} & \boldsymbol{E}_{12} \\ \boldsymbol{E}_{21} & \boldsymbol{E}_{22} \end{bmatrix}$, the 2×2 DtN impedance matrix $\boldsymbol{Z}$ $(r\boldsymbol{\Sigma}_n = \boldsymbol{Z}\boldsymbol{u}_n)$ propagates outward via the unconditionally stable Möbius transformation

$$\boldsymbol{Z}(r_{i+1}) = (\boldsymbol{E}_{21} + \boldsymbol{E}_{22}\boldsymbol{Z}(r_i))(\boldsymbol{E}_{11} + \boldsymbol{E}_{12}\boldsymbol{Z}(r_i))^{-1}. \tag{12}$$

For a scalar isotropic layer $\boldsymbol{C}_i = a_i\boldsymbol{C}_0$, the similarity relation $\boldsymbol{N}_n(a_i\boldsymbol{C}_0) = \boldsymbol{D}(a_i)\boldsymbol{N}_n(\boldsymbol{C}_0)\boldsymbol{D}(a_i)^{-1}$ with $\boldsymbol{D}(a_i) = \mathrm{diag}(1,1,a_i,a_i)$ yields $\boldsymbol{Z}(r_{i+1}) = a_i\,\boldsymbol{Z}^{(0)}(r_{i+1};\, a_i^{-1}\boldsymbol{Z}(r_i))$ under Equation (12). This scaling allows batched impedance propagation across $n = 0, \ldots, 64$ in 0.72ms (a $189\times$ speedup, matching direct assembly to 2.5×10^{-14}).

2. Analytical proof of the general isotropic high-order floor (e_1, e_2, h_∞)

For an isotropic medium with shear modulus μ and Kolosov constant $\kappa = 1 + 2\mu/K$, the cylindrical moduli take the form $C_{rr} = C_{\theta\theta} = \mu(\kappa+1)/(\kappa-1)$, $C_{r\theta} = \mu(3-\kappa)/(\kappa-1)$, $c = (3-\kappa)/(\kappa+1)$, and $E_s = 8\mu/(\kappa+1)$. Evaluating the background eigenvectors $\boldsymbol{Y}_{\pm}(n)$ (Supplementary Note 2) in the orthonormal rotated basis $\boldsymbol{Q} = \frac{1}{\sqrt{2}}\begin{bmatrix} 1 & 1 \\ -1 & 1 \end{bmatrix}$ $(\boldsymbol{v}_- = \boldsymbol{Q}_{:,1},\ \boldsymbol{v}_+ = \boldsymbol{Q}_{:,2})$ yields the exact finite-order diagonalized disc and unbounded-exterior impedances $\boldsymbol{Q}^{\mathrm{T}}\boldsymbol{Z}_{\mathrm{in}}(n)\boldsymbol{Q} = 2\mu_0\mathrm{diag}(n-1, (n+1)/\kappa_0)$ and $\boldsymbol{Q}^{\mathrm{T}}\boldsymbol{Z}_{\mathrm{ext}}^{\infty}(n,b)\boldsymbol{Q} = 2\mu_0\mathrm{diag}((n-1)/\kappa_0, n+1)$, making the $O(1/n)$ curvature corrections explicit. Scaling the impedance by n $(\widetilde{\boldsymbol{Z}} = \boldsymbol{Z}/n)$, the leading $O(n)$ algebraic Riccati equation for $\widetilde{\boldsymbol{Z}}_{\mathrm{in}}$ as $n \to \infty$ becomes

$$\boldsymbol{A}_{21} + \boldsymbol{A}_{22}\widetilde{\boldsymbol{Z}} - \widetilde{\boldsymbol{Z}}\boldsymbol{A}_{11} - \widetilde{\boldsymbol{Z}}\boldsymbol{A}_{12}\widetilde{\boldsymbol{Z}} = \boldsymbol{0},\ \boldsymbol{A}_{11} = \begin{bmatrix} 0 & -c \\ 1 & 0 \end{bmatrix},\ \boldsymbol{A}_{12} = \mathrm{diag}(C_{11}^{-1}, \mu^{-1}),\ \boldsymbol{A}_{21} = \mathrm{diag}(0, E_s),\ \boldsymbol{A}_{22} = -\boldsymbol{A}_{11}^{\mathrm{T}}, \tag{13}$$

which Equation (4) satisfies with identically zero residual. In the $\boldsymbol{Q}$ basis, all three leading $O(n)$ half-plane impedances diagonalize simultaneously:

$$\boldsymbol{Q}^{\mathrm{T}}\widetilde{\boldsymbol{Z}}_{\mathrm{in}}\boldsymbol{Q} = 2\mu_0\mathrm{diag}(1, \kappa_0^{-1}),\quad \boldsymbol{Q}^{\mathrm{T}}\widetilde{\boldsymbol{Z}}_{\mathrm{ext}}\boldsymbol{Q} = 2\mu_0\mathrm{diag}(\kappa_0^{-1}, 1),\quad \boldsymbol{Q}^{\mathrm{T}}\widetilde{\boldsymbol{Z}}_{L}\boldsymbol{Q} = 2\mu_L\mathrm{diag}(1, \kappa_L^{-1}). \tag{14}$$

Substituting Equation (14) into $\boldsymbol{S}_C = (\widetilde{\boldsymbol{Z}}_L + \widetilde{\boldsymbol{Z}}_{\mathrm{ext}})^{-1}(\widetilde{\boldsymbol{Z}}_{\mathrm{in}} - \widetilde{\boldsymbol{Z}}_L)$ yields the two principal scattering eigenvalues

$$s_- = \frac{\kappa_0(\mu_0 - \mu_L)}{\kappa_0\mu_L + \mu_0},\quad s_+ = \frac{\mu_0\kappa_L - \mu_L\kappa_0}{\kappa_0(\mu_L + \mu_0\kappa_L)}, \tag{15}$$

Weighting $s_{\mp}^2$ by the exterior-to-interior energy ratios $(\tilde{z}_{\mathrm{ext},\mp}/\tilde{z}_{\mathrm{in},\mp}) = (\kappa_0^{-1}, \kappa_0)$ directly gives $e_1 = \kappa_0^{-1}s_-^2$ and $e_2 = \kappa_0 s_+^2$ in Equation (5). For a concentrated ring source in the pressed limit $r_c \to b^+$, the admittance metric $\widetilde{\boldsymbol{Y}}^{-1} = 2\mu_0(1 + \kappa_0^{-1})\boldsymbol{I}_2$ assigns modal weights $\kappa_0/(\kappa_0+1)$ and $1/(\kappa_0+1)$, proving Equation (6).

3. Analytical proof and admissibility conditions of the all-order neutral polar-orthotropic ring theorem

For an isotropic background (K_0, μ_0), positive definiteness of $\boldsymbol{C}^{(m)}$ requires $s_{11}^{(m)} > |s_{12}^{(m)}|$ and $s_{66}^{(m)} > 0$. Substituting $s_{11}^{(0)} = 1/E_s^{(0)}$ and $s_{12}^{(0)} = -c^{(0)} s_{11}^{(0)}$ (with $c^{(0)} = \nu_0$) into Equation (8) gives $c^{(m)} = -s_{12}^{(m)}/s_{11}^{(m)} = 1 - n_S(1-\nu_0)$, $s_{66}^{(m)}/s_{11}^{(m)} = 4n_S^2 - 2n_S(1-\nu_0)$, and $s_{11}^{(m)} - |s_{12}^{(m)}| > 0 \Leftrightarrow 1 + c^{(m)} = 2 - n_S(1-\nu_0) > 0$. Combining $4n_S^2 - 2n_S(1-\nu_0) > 0$ with $2 - n_S(1-\nu_0) > 0$ establishes the necessary and sufficient thermodynamic stability window $(1-\nu_0)/2 < n_S < 2/(1-\nu_0)$ (Equation 9).

For every integer $n \geq 2$, the background system matrix $\boldsymbol{N}_n^{(0)}$ has four distinct real eigenvalues $\{n+1, n-1, -n-1, -n+1\}$, whose eigenvectors span $\boldsymbol{Y}_+(n) = [\boldsymbol{y}_{n+1}, \boldsymbol{y}_{n-1}]$ and $\boldsymbol{Y}_-(n) = [\boldsymbol{y}_{-n-1}, \boldsymbol{y}_{-n+1}]$. Substituting Equation (8) into Equation (11) gives $E_s^{(m)} = n_S E_s^{(0)}$ and $1/C_{rr}^{(m)} = (1 - (c^{(m)})^2)/(n_S E_s^{(0)})$. Constructing denominator-free polynomial bases from $\ker(\boldsymbol{N}_n^{(0)} \mp (n \pm 1)\boldsymbol{I})$ satisfying $\det \boldsymbol{Y}_{\pm,1:2}(n) = \pm 2(K_0 + 2\mu_0) \neq 0$, symbolic algebra in SymPy (Supplementary Note 2, Equations S5–S8) proves identically for all $n \geq 2$ that $\boldsymbol{N}_n^{(m)} \boldsymbol{Y}_\pm(n) = \boldsymbol{Y}_\pm(n) \boldsymbol{\Lambda}_\pm(n)$, where the 2×2 block generators satisfy $\mathrm{tr}\boldsymbol{\Lambda}_\pm(n) = \pm 2nn_S$ and $\det \boldsymbol{\Lambda}_\pm(n) = n^2 - 1$. Their internal exponents form a complex-conjugate pair when $(1-\nu_0)/2 < n_S < \sqrt{1 - 1/n^2}$ and become distinct real pairs above this threshold. Independent exact rational rank checks confirm 0/504 failures across $2 \leq n \leq 101$. Consequently, the layer propagator $\boldsymbol{E}_m = \exp(\boldsymbol{N}_n^{(m)} \ln(r_2/r_1))$ preserves $\mathrm{span}(\boldsymbol{Y}_\pm(n))$ for any $r_2 > r_1 > 0$. At $n = 0$ and $n = 1$, exact rank checks on the explicit regular and decaying/Kelvinlet bases (Supplementary Note 2) confirm invariance of $\mathcal{V}_+(0)$ and $\mathcal{V}_+(1)$ (18/18 cases), whereas $\mathcal{V}_-(0)$ and the logarithmic Kelvinlet generalized mode $\boldsymbol{y}_{\mathrm{kel}}(r) = \boldsymbol{v}_{\mathrm{kel}} + \ln r\, \boldsymbol{v}_{\mathrm{tr}}$ are non-invariant whenever $n_S \neq 1$ (18/18 cases).

4. Angularly coupled Fourier–Toeplitz transfer method

When the layer stiffness $a_i(\theta)$ varies across 192 angular sectors in layer i, angular harmonics $e^{\mathrm{i}k\theta}$ couple through the $m \times m$ Toeplitz matrices $\boldsymbol{A}_i = \mathrm{Toep}(\widehat{a_i})$ and $\boldsymbol{B}_i = \mathrm{Toep}(\widehat{a_i^{-1}})$. Using cutoff $|k| \leq K_c = 80$ gives $m = 2K_c + 1 = 161$ modes, $4m \times 4m = 644 \times 644$ layer state matrices, and $2m \times 2m = 322 \times 322$ impedance blocks; for the high-resolution $K \leq 128$ benchmark, we raise the cutoff to $K_c = 150$. The resulting coupled layer system matrix is

$$\boldsymbol{N}_{\mathrm{cpl},i} = \begin{bmatrix} -c\boldsymbol{I}_m & -c\boldsymbol{D} & C_{11}^{-1}\boldsymbol{B}_i & \boldsymbol{0} \\ -\boldsymbol{D} & \boldsymbol{I}_m & \boldsymbol{0} & G^{-1}\boldsymbol{B}_i \\ E_S\boldsymbol{A}_i & E_S\boldsymbol{A}_i\boldsymbol{D} & c\boldsymbol{I}_m & -\boldsymbol{D} \\ -E_S\boldsymbol{D}\boldsymbol{A}_i & -E_S\boldsymbol{D}\boldsymbol{A}_i\boldsymbol{D} & -c\boldsymbol{D} & -\boldsymbol{I}_m \end{bmatrix}, \quad \boldsymbol{D} = \mathrm{diag}(\mathrm{i}k)_{k=-K_c}^{K_c}, \tag{16}$$

and the coupled DtN impedance matrix $\boldsymbol{Z}_C$ propagates outward via Equation (12).

5. Inverse optimization formulations, load-space bases, and discrete-beam lattice FEM

Radial hat profile and load-space definitions. Across all continuum and finite-element near-field benchmarks, the radial support of body-force loads is defined by the piecewise-linear hat profile

$$\psi(r; r_c, w) = \max\left(0, 1 - \frac{|r - r_c|}{w}\right), \quad \mathrm{supp}\psi = [r_c - w, r_c + w]. \tag{17}$$

On the square plate $[-75,75]^2$mm, each raw load family is whitened via eigendecomposition of its intact-plate elastic energy Gram matrix $\boldsymbol{G}_0 = \boldsymbol{U}_0^{\mathrm{T}}\boldsymbol{K}_0\boldsymbol{U}_0$, retaining modes above $10^{-10}\lambda_{\max}(\boldsymbol{G}_0)$ (or $10^{-8}\lambda_{\max}$ for boundary displacements; see Supplementary Note 5 for full basis dimensions):

- *Boundary displacement spaces:* P_4 consists of all 25 bivariate monomials $(x/L)^i(y/L)^j$ $(i+j \le 4)$ on both (u_x, u_y) boundary components (50 raw modes). The training boundary space $\mathcal{L}_{\mathrm{BD}}^{(\mathcal{C})}$ combines Legendre products $P_i(x/L)P_j(y/L)$ $(i+j \le 10)$ with perimeter arc-length Fourier harmonics $k \le 32$ on both components (262 raw modes). Full T6 boundary verification (BD) spans all outer-boundary nodal trace DOFs. On the circular plate, $\mathcal{L}_{\mathrm{BD}}$ spans all regular Dirichlet modes up to $n \le 12$.
- *Polynomial exterior body-force space ($\mathcal{L}_{\mathrm{BF}}$):* Bivariate monomial body forces $(x/L)^i(y/L)^j$ $(i+j \le 6)$ of total degree ≤ 6 on both (f_x, f_y) components (56 raw modes), supported on $\Omega_{\mathrm{obs}} = \{r > b\}$ with clamped outer edges.
- *Near-field ring classes:* Radial body forces $\boldsymbol{f}(r,\theta) = \psi(r; r_c, w)\cos/\sin(k\theta)\,\boldsymbol{e}_a$ $(a \in \{x,y\}, k \le K)$ with clamped outer boundaries, tested across wide $(r_c = 60, w = 5\mathrm{mm})$, offset $(r_c = 63, w = 5\mathrm{mm})$, half-width $(r_c = 57.5, w = 2.5\mathrm{mm})$, thin $(w = 0.3125\mathrm{mm})$, and ultrathin $(w = 0.15625\mathrm{mm})$ shells at angular cutoffs $K \in \{48,64,96,128\}$.
- *Eight physical boundary loads (Results Section 6):* Prescribed affine boundary displacements $\boldsymbol{u}|_{\partial\Omega} = \boldsymbol{E}\boldsymbol{x}$ comprising five normal-strain ratios $\varepsilon_{yy}/\varepsilon_{xx} \in \{0.8,0.9,1.0,1.1,1.25\}$ $(\gamma_{xy} = 0$, where $\varepsilon_{yy}/\varepsilon_{xx} = 1.0$ defines $R_{\mathrm{biax}})$ and three combined biaxial–shear loads $(\varepsilon_{xx} = \varepsilon_{yy} = 1$, $\gamma_{xy} \in \{0.05,0.10,0.20\})$, supplemented by pure uniaxial x tension $(\varepsilon_{xx} = 1, \varepsilon_{yy} = \gamma_{xy} = 0 \Longrightarrow R_{\mathrm{ux}})$ and pure shear $(\gamma_{xy} = 1, \varepsilon_{xx} = \varepsilon_{yy} = 0 \Longrightarrow R_{\mathrm{shear}})$.

Square-plate 20×192 inverse optimization. The design variables $\boldsymbol{z} \in \mathbb{R}^{3840}$ are defined on a 20×192 radial–angular Q4 grid (2 × mesh: $m = 48, n_{r1} = 20, n_{r2} = 32$) and mapped to element stiffness multipliers through a linear density cone filter $\boldsymbol{P}$ of radius $R_F = 3.0\mathrm{mm}$ [39, 40] followed by a logistic-exponential projection $a_e(\boldsymbol{z}) = a_{\min}\exp[\ln(a_{\max}/a_{\min})(\boldsymbol{P}\sigma(\boldsymbol{z}))_e]$ (with $[a_{\min}, a_{\max}] = [0.02,4.0]$ or $[0.71,2.45]$). Forward solves and exact adjoint sensitivities are computed on a nested 6 × Q4 mesh ($m = 144, n_{r1} = 60, n_{r2} = 96$):

1. *Trained-6:* Minimizes the summed cloak-to-bare-hole exterior error energy across the top 6 bare-hole eigenvectors of $\boldsymbol{G}_V$ in P_4, solved with L-BFGS-B starting from $a = 1$ plus two randomized initializations.
2. *BC-cloak, Joint-cloak, Nominal-bounded, and Robust-bounded:* Minimize a smooth Schatten-p $(p = 8)$ upper bound on the worst-case boundary error operator $\boldsymbol{G}_{C,\mathcal{C}}(\boldsymbol{z})$, subject to multi-geometry minimax log-barrier non-deterioration constraints over the training space $\mathcal{L}_{\mathrm{tr}}$ ($\mathcal{L}_{\mathrm{BD}}^{(\mathcal{C})}$ for BC-cloak; $[\mathcal{L}_{\mathrm{BD}}^{(\mathcal{C})}|\mathrm{NF}_{55\text{–}65}(K = 48)]$ for Joint-cloak, Nominal-bounded, and 4-geometry Robust-bounded):

$$\min_{\boldsymbol{z}} \left(\sum_j \lambda_j(\boldsymbol{G}_{C,\mathcal{C}}(\boldsymbol{z}))^p \right)^{1/p} - \mu \sum_{g\in\mathcal{G}} \sum_i \ln\left(\tau_{cap} - \lambda_i\left(\frac{\boldsymbol{G}_C^{(g)}(\boldsymbol{z}) - \boldsymbol{G}_V^{(g)}}{\ell_V} \right) \right), \tag{18}$$

Equation (18) is solved via a 4-stage barrier continuation $\mu/\tau_{cap} \in \{33.3,3.33,0.333,0.0333\}$ ($\tau_{cap} = 0.7\tau_d$, where τ_d denotes the design acceptance tolerance) using limited-memory BFGS ($m = 20$, backtracking Armijo line search, up to 750 iterations per stage [41]), initialized from the feasible baseline $a = 1$.

Circular-plate 20-layer epigraph minimax optimization (Table 4). For axisymmetric 20-layer scalar stiffness profiles $a \in [0.02,4.0]^{20}$, epigraph SLSQP solves

$$\min_{a,\eta} \eta \ \text{s.t.}\ E_n(a) \le \eta \ \ (n \le 12), \quad h_n^{\mathrm{BD}}(a) \le h_{\mathrm{cap}} \ \ (n \le 12), \tag{19}$$

with optional joint constraints $h_n^{55-65}(a) \le 0.7\tau$ ($n \le 64$), a fixed outer buffer $a_{20-n_{\mathrm{fix}}+1:20} = 1$, a smooth 4-layer cosine taper $a_{16+k} = 1 + (a_{16} - 1)\cos^2(k\pi/8)$ ($k = 1, \ldots, 4$), or a 2-layer Suo-matched shell ($n_S = 1.2$). Sweeping $h_{\mathrm{cap}} \in \{0.7\tau, 10\tau, 50\tau, \infty\}$ traces the Pareto frontier (Supplementary Note 5).

2D discrete Timoshenko and Euler–Bernoulli beam FEM (Results Section 7). Individual lattice strut widths ($H_{31\times30}, V_{30\times31}$) were measured directly over the central 40% span of each bar from 1500×1500 geometry bitmaps (pixel size 0.1mm, lattice pitch $\ell = 150/31 \approx 4.839$mm, background width $b_0 = 0.938$mm, with outer platen frame members fixed to b_0). The 31×31-node frame (961 nodes, 2,883 DOFs $[u_x, u_y, \theta_z]$, 1,628 active bars for the void and cloaks, and 564 cloak bars in 30–55mm) was assembled using exact 2D Timoshenko beam elements ($E = 1$, $\nu_s = 0.33$, shear correction factor $k_s = 5/6$, shear parameter $\Phi = 12EI/(k_s GA\ell^2)$) as well as slender Euler–Bernoulli beam elements ($\Phi = 0$). Exterior strain energy was summed over all active bars whose midpoints lie in $r > 55$mm.

6. Independent T6 finite-element verification, mesh/quadrature convergence, and polar harmonic projection

Independent verification was carried out on 6-node quadratic triangular (T6) meshes distinct from the Q4 optimization grids. At the finest mesh level (567,938 DOFs, 283,104 T6 elements, and 2,304 trace DOFs on $r = 55$mm), exact Schur-complement reduction onto $r = 55$mm assembled the trace stiffness $\boldsymbol{M}_{\mathrm{tr}}$ and load-transfer operator $\boldsymbol{R}_{\mathcal{L}} = \boldsymbol{T}_{\mathcal{L}} \boldsymbol{G}_{\mathcal{L}}^{-1/2}$ (truncated at $10^{-10}\lambda_{\max}(\boldsymbol{G}_{\mathcal{L}})$) once per background. Worst-case deterioration was then evaluated directly as $h(\mathcal{L}) = \lambda_{\max}(\boldsymbol{R}_{\mathcal{L}}^{\mathrm{T}} \boldsymbol{M}_{\mathrm{tr}} \boldsymbol{R}_{\mathcal{L}})/\ell_V$.

Mesh convergence and 6-point versus 150-point triangle quadrature checks were performed across three mesh densities (252,674 DOFs, 350,978 DOFs with exterior radial refinement, and 567,938 DOFs; Supplementary Note 3, Supplementary Fig. S2, and Supplementary Tables S2a–b). The dominant FE harmonic orders n^* reported in Tables 2–3 and Supplementary Table S1 were extracted by projecting polar tractions (t_r, t_θ) onto Fourier modes via trapezoidal-angle-weighted least squares on the non-uniform circular trace nodes (condition number 1.416).

For the 13 localized self-equilibrated finite-arc patches, load vectors were integrated on the 567,938-DOF mesh using 150-point sub-triangle quadrature with discrete orthogonalized rigid-body equilibrium ($\max(|F_x|, |F_y|, |M_z|/b)/\|\boldsymbol{f}\|_{L^1} < 10^{-13}$). These FE results were compared directly against zero-parameter continuum theory ($n \in [0,220]$) computed via exact regular eigenvector propagation $\boldsymbol{U}_+(n)\mathrm{diag}(q^{n+1}, q^{n-1})\boldsymbol{U}_+(n)^{-1}$ ($n \ge 2$) to avoid float64 cancellation at high n. Note that circular-plate optimizations normalize energy by the analytical circular reference visibility ℓ_V (yielding 2.849τ for the 2.5mm buffer on $\nu_0 = 0.60$), whereas square-plate comparisons normalize by the square-plate FE bare-hole reference $\ell_V = 0.103681$ (2.834τ predicted vs. 3.05τ FE at $n^* = 6$). Extended derivations, optimization details, convergence tables, domain-size scaling analyses, localized patch results, and discrete-beam lattice benchmarks are provided in Supplementary Notes 1–6, Supplementary Figures S1–S3, and Supplementary Tables S0–S5.

7. Code and data availability

All analytical solvers, Q4 inverse-optimization scripts, T6 finite-element verification codes, 2D discrete-beam lattice solvers, optimized design arrays, and figure-generation modules required to reproduce every

quantitative result and figure are included in the accompanying reproduction archive (reproduction_archive.zip; documented in Supplementary Note 6). The archive is available to editors and reviewers during peer review and will be deposited in a public repository with a permanent DOI upon publication.

Acknowledgements, Author Contributions, and Competing Interests

- **Acknowledgements:** This work was sponsored by the Fujian Provincial Health Technology Project (Grant No. 2024GGA052).

- **Author Contributions:** Guangtao Wei: Conceptualization; Methodology; Software; Validation; Formal analysis; Investigation; Data curation; Writing – original draft; Writing – review & editing; Visualization; Supervision. Miao Yu: Investigation; Software; Validation. Jun Liu: Conceptualization; Funding acquisition; Project administration.
- **Competing Interests:** The authors declare no competing interests.

Main Tables

Table 1 | Exact closed-form high-order reflection floor (e_1, e_2) vs. numerical state-space transfer ($n = 160$)

Outer-layer / Background case	μ_L/μ_0	K_L/K_0	κ_0	κ_L	Exact formula (e_{min}, e_{max})	State-space n=160 (e_{min}, e_{max})	Max relative error
v_0 = 0.60 general pair 1	1.50	1.000	1.500	1.750	(1.57791× 10^{-2}, 3.55030× 10^{-2})	(1.57791× 10^{-2}, 3.55030× 10^{-2})	5.4 × 10^{-13}
v_0 = 0.60 general pair 2	1.00	2.000	1.500	1.250	(0, 8.23045× 10^{-3})	(2.6 × 10^{-19}, 8.23045× 10^{-3})	5.1 × 10^{-13}
v_0 = 0.60 general pair 3	1.00	0.375	1.500	2.333	(0, 4.16667× 10^{-2})	(−2.9 × 10^{-20}, 4.16667× 10^{-2})	2.1 × 10^{-13}
v_0 = 0.60 general pair 4	2.00	0.500	1.500	3.000	(0, 9.37500× 10^{-2})	(4.3 × 10^{-18}, 9.37500× 10^{-2})	3.3 × 10^{-13}
v_0 = 0.60 general pair 5	0.50	2.500	1.500	1.100	(3.19010× 10^{-2}, 1.22449× 10^{-1})	(3.19010× 10^{-2}, 1.22449× 10^{-1})	3.3 × 10^{-13}
v_0 = 0.60 general pair 6	2.50	0.250	1.500	6.000	(4.67128× 10^{-2}, 1.49584× 10^{-1})	(4.67128× 10^{-2}, 1.49584× 10^{-1})	2.5 × 10^{-13}
v_0 = 0.60 general pair 7 (scalar a=1.20)	1.20	1.200	1.500	1.500	(7.65306× 10^{-3}, 8.23045× 10^{-3})	(7.65306× 10^{-3}, 8.23045× 10^{-3})	1.2 × 10^{-12}
v_0 = 0.60 general pair 8	0.25	1.125	1.500	1.111	(1.94988× 10^{-1}, 4.46281× 10^{-1})	(1.94988× 10^{-1}, 4.46281× 10^{-1})	1.8 × 10^{-13}
Scalar v_0 = 0.60 (a=2.00)	2.00	2.000	1.500	1.500	(9.37500× 10^{-2}, 1.22449× 10^{-1})	(9.37500× 10^{-2}, 1.22449× 10^{-1})	2.4 × 10^{-12}
Scalar auxetic v_0 = −0.80 (a=1.20)	1.20	1.200	19.000	19.000	(1.34171× 10^{-3}, 1.86256× 10^{-3})	(1.34171× 10^{-3}, 1.86256× 10^{-3})	8.2 × 10^{-14}
Scalar v_0 = 0.33 (a=1.20)	1.20	1.200	2.008	2.008	(6.90971× 10^{-3}, 7.80515× 10^{-3})	(6.90971× 10^{-3}, 7.80515× 10^{-3})	2.6 × 10^{-12}
Suo-matched v_0 = 0.60 (n_S=1.2, $C_{11}^{(0)}$=1)	G/μ_0=0.800	orthotropic (C_{rr}=$C_{\theta\theta}$=1.053, $C_{r\theta}$=0.547)	1.500	orthotropic	(0, 0) (all-order $n \geq 2$ neutral)	< 10^{-28} (n=32), < 10^{-29} ($n \geq 64$)	Exact 0

***Note:** The three scalar-contrast rows (a = 2.00 on $\nu_0 = 0.60$, a = 1.20 on $\nu_0 = -0.80$, and a = 1.20 on $\nu_0 = 0.33$) are representative examples from the 18 scalar-contrast cases (36 nonzero eigenvalues) plotted in Fig. 1c. Across all 18 cases, the maximum relative error between Equation (5) and numerical state-space transfer at n = 160 is 8.19 × 10^{-11}.

Table 2 | Zero-parameter continuum (1D mean) and angularly coupled ($|k| \le 80$) theory vs. T6 FE across radial load classes

Background & Design	Outer layer $\bar{a}_{20} \pm \sigma_\theta$	Wide ring (55–65 mm) 1D | Coupled | FE	Half-width (55–60 mm) 1D | Coupled | FE	Thin ring (55.31 mm) 1D | Coupled | FE	Dominant polar order n^* (1D | FE)
v_0=−0.80 Joint-cloak (τ_d=10^{-3})	1.189 ± 0.003	7.02×10^{-4} | 7.32×10^{-4} | 6.48×10^{-4}	9.87×10^{-4} | 1.03×10^{-3} | 9.02×10^{-4}	2.22×10^{-3} | 2.37×10^{-3} | 2.40×10^{-3}	35 | 34 (thin)
v_0=−0.80 BC-cloak (τ_d=10^{-3})	1.213 ± 0.041	6.31×10^{-3} | 6.94×10^{-3} | 5.61×10^{-3}	8.44×10^{-3} | 9.31×10^{-3} | 7.40×10^{-3}	1.10×10^{-2} | 1.21×10^{-2} | 9.51×10^{-3}	5 | 5 (thin/wide)
v_0=−0.80 Joint-cloak (τ_d=10^{-4})	1.001 ± 0.002	6.98×10^{-5} | 7.00×10^{-5} | 6.82×10^{-5}	1.29×10^{-4} | 1.30×10^{-4} | 1.28×10^{-4}	2.49×10^{-4} | 2.52×10^{-4} | 2.51×10^{-4}	13 | 13 (thin)
v_0=−0.80 BC-cloak (τ_d=10^{-4})	1.411 ± 0.024	8.58×10^{-4} | 8.94×10^{-4} | 8.88×10^{-4}	2.02×10^{-3} | 2.13×10^{-3} | 2.13×10^{-3}	7.13×10^{-3} | 7.61×10^{-3} | 7.69×10^{-3}	38 | 39 (thin)
v_0=0.60 Joint-cloak (τ_d=10^{-3})	0.996 ± 0.038	1.00×10^{-2} | 1.54×10^{-3} | 7.61×10^{-4}	1.21×10^{-2} | 2.28×10^{-3} | 1.25×10^{-3}	1.40×10^{-2} | 3.48×10^{-3} | 2.40×10^{-3}	6 | 9 (thin)
v_0=0.60 BC-cloak (τ_d=10^{-3})	1.054 ± 0.309	2.45×10^{-2} | 4.22×10^{-2} | 4.24×10^{-2}	3.00×10^{-2} | 1.01×10^{-1} | 1.01×10^{-1}	3.57×10^{-2} | 3.75×10^{-1} | 3.81×10^{-1}	1 | 45 (thin)
v_0=0.60 Joint-cloak (τ_d=10^{-4})	1.008 ± 0.009	3.92×10^{-3} | 7.73×10^{-5} | 7.63×10^{-5}	4.97×10^{-3} | 2.51×10^{-4} | 2.52×10^{-4}	6.04×10^{-3} | 9.21×10^{-4} | 9.23×10^{-4}	7 | 55 (thin)
v_0=0.60 BC-cloak (τ_d=10^{-4})	1.415 ± 0.109	5.93×10^{-2} | 2.38×10^{-2} | 2.38×10^{-2}	7.31×10^{-2} | 5.15×10^{-2} | 5.14×10^{-2}	8.70×10^{-2} | 1.46×10^{-1} | 1.47×10^{-1}	6 | 41 (thin)
v_0=0.60 Trained-6 (6-load)	0.155 ± 0.012	7.71×10^{-1} | 7.94×10^{-1} | 7.97×10^{-1}	1.33 | 1.39 | –	2.94 | 3.12 | –	20 | 19 (wide)
v_0=0.33 BC-cloak (τ_d=10^{-3})	0.901 ± 0.053	2.58×10^{-2} | 9.87×10^{-3} | 9.91×10^{-3}	3.36×10^{-2} | 2.31×10^{-2} | –	4.26×10^{-2} | 7.46×10^{-2} | –	2 | 19 (wide)
v_0=0.33 BC-cloak (τ_d=10^{-4})	1.467 ± 0.089	4.37×10^{-2} | 1.10×10^{-2} | 1.09×10^{-2}	5.61×10^{-2} | 2.65×10^{-2} | –	8.26×10^{-2} | 1.23×10^{-1} | –	6 | 23 (wide)

Table 3 | Independent 567,938-DOF T6 finite-element verification across thin/ultrathin contact rings

Background & Design	Design τ_d / note	Bound. disp. (h/τ_d)	Wide ring 55–65 mm	Thin w=0.31 mm (K=64)	Thin w=0.31 mm (K=96)	Thin w=0.31 mm (K=128)	Ultrathin w=0.16 mm (K=64)	Ultrathin w=0.16 mm (K=96)	Ultrathin w=0.16 mm (K=128)	FE / Theory ratio, polar n^*, & 150-pt check
v_0=−0.80 Joint-cloak	$\tau_d = 10^{-3}$	0.543	0.648	2.39	2.39	2.39	2.78	2.78	2.78	1.000–1.005× (thinning × 1.165; n^*=33–42; 150pt 2.804τ)
v_0=−0.80 Joint-cloak	$\tau_d = 10^{-4}$	0.536	0.682	2.51	2.51	2.51	2.64	2.64	2.64	0.995× (K-sat × 1.000002; thinning × 1.056; n^*=13; 150pt 2.645τ)
v_0=−0.80 BC-cloak	$\tau_d = 10^{-4}$	0.701	8.88	76.3	76.3	76.3	91.7	91.8	91.8	1.003–1.006× (thinning × 1.203; n^*=38–53; 150pt 91.75τ)
v_0=−0.80 Nominal-bounded	$\tau_d = 10^{-3}$	0.544	0.648	1.68	1.71	1.73	2.05	2.14	2.23	1.005–1.026× (K-sat × 1.090; thinning × 1.287; n^*=35–50; 150pt 2.227τ)
v_0=−0.80 Robust-bounded	$\tau_d = 10^{-3}$ (nom. circle)	0.543	0.213	0.830	0.830	0.830	0.975	0.977	**0.977**	1.001–1.004× (2.3% below τ, th 0.973τ, n^*=32–44, 150pt 0.976τ)
v_0=0.60 Unbuffered BC-cloak	$\tau = 10^{-3}$ (w_{buf}=0)	0.581	13.76	137.8	144.3	148.0	178.0	180.0	182.4	0.997–1.003× (polar n^* = 63 → 121; 150pt 184.45τ)

Background & Design	Design τ_d / note	Bound. disp. (h/τ_d)	Wide ring 55–65 mm	Thin w=0.31 mm (K=64)	Thin w=0.31 mm (K=96)	Thin w=0.31 mm (K=128)	Ultrathin w=0.16 mm (K=64)	Ultrathin w=0.16 mm (K=96)	Ultrathin w=0.16 mm (K=128)	FE / Theory ratio, polar n^*, & 150-pt check
v_0=0.60 Buffered BC-cloak	$\tau = 10^{-3}$ (w_{buf}=2.5 mm)	0.581	1.95	**3.05**	**3.05**	**3.05**	**3.09**	**3.09**	**3.09**	Low-n^* sq. offset 1.075–1.076× (n^*=6); **−48.6× drop; span 1.015×**
v_0=0.60 Unbuffered Joint-cloak	$\tau = 10^{-3}$ (w_{buf}=0)	0.391	0.954	6.32	6.43	6.81	8.16	8.17	8.33	0.998–1.004× (polar n^* = 48 → 127; 150pt 8.392τ)
v_0=0.60 Buffered Joint-cloak	$\tau = 10^{-3}$ (w_{buf}=2.5 mm)	0.377	0.966	**1.63**	**1.63**	**1.63**	**1.65**	**1.65**	**1.65**	Low-n^* sq. offset 1.341–1.342× (n^*=2); **−4.2× drop; span 1.018×**

Table 4 | Effect of outer background buffer, Pareto boundary constraints, smooth cosine taper, and Suo-matched orthotropic shell ($E_{\max,C}$ over full $\mathcal{L}_{\mathrm{BD}}\ n \le 12$; Suo moduli normalized to $C_{11}^{(0)} = 1$)

Background & Tolerance τ	Design strategy	$E_{max,C}$	h_{BD}/τ	Wide ring 55–65 mm (n^*)	Thin ring w=0.31 mm,K=64 (n^*)	Pressed-ring floor h_∞/τ	Outer 4 layers [a_{17}, a_{18}, a_{19}, a_{20}]
v_0=0.60 (τ=10^{-3})	Trained (unconstrained, 0 mm buf)	0.305	169.0	477.6 (16)	1306.8 (28)	36.13	[4.000, 4.000, 0.057, 1.178]
v_0=0.60 (τ=10^{-3})	Trained (unconstrained) + 2.50 mm buffer	0.345	108.8	307.6 (14)	701.4 (19)	**0.00**	[4.000, 0.062, 1.000, 1.000]
v_0=0.60 (τ=10^{-3})	Relaxed boundary ($h_{BD} \le 50\tau$, 0 mm buf)	0.306	50.0	364.6 (18)	1026.0 (25)	781.11	[4.000, 4.000, 0.058, 2.357]
v_0=0.60 (τ=10^{-3})	Relaxed boundary ($h_{BD} \le 50\tau$) + 2.50 mm buf	0.390	50.0	164.5 (13)	344.4 (15)	**0.00**	[0.070, 1.075, 1.000, 1.000]
v_0=0.60 (τ=10^{-3})	Strict boundary repair (0 mm buf)	0.864	0.70	13.83 (29)	137.80 (64)	270.00	[1.064, 1.109, 1.425, 0.652]
v_0=0.60 (τ=10^{-3})	Boundary + 1.25 mm buffer	0.866	0.70	2.54 (6)	10.39 (52)	**0.00**	[1.121, 1.329, 0.706, 1.000]
v_0=0.60 (τ=10^{-3})	Boundary + 2.50 mm buffer	0.867	0.70	1.78 (6)	**2.85** (6)	**0.00**	[1.101, 0.896, 1.000, 1.000]
v_0=0.60 (τ=10^{-3})	Smooth 4-layer cosine taper	0.867	0.70	1.65 (6)	**2.55** (6)	**0.00**	[0.992, 0.995, 0.999, 1.000]
v_0=0.60 (τ=10^{-3})	Mixed: 18 scalar + 2 Suo (n_S=1.2)	**0.857**	0.70	1.15 (2)	**2.61** (26)	**0.00**	18 scalar + 2 Suo (C_{rr}=1.053, G=0.160)
v_0=0.60 (τ=10^{-3})	Joint (55–65) + 2.50 mm buffer	0.879	0.70	0.70 (6)	**1.22** (2)	**0.00**	[0.925, 1.085, 1.000, 1.000]
v_0=0.33 (τ=10^{-3})	Boundary repair (0 mm buf)	0.860	0.70	2.26 (25)	34.36 (63)	68.31	[1.131, 1.170, 1.164, 0.799]
v_0=0.33 (τ=10^{-3})	Boundary + 2.50 mm buffer	0.862	0.70	1.30 (6)	**2.02** (6)	**0.00**	[1.107, 1.019, 1.000, 1.000]
v_0=0.33 (τ=10^{-3})	Mixed: 18 scalar + 2 Suo (n_S=1.2)	**0.850**	0.70	1.12 (6)	**1.79** (2)	**0.00**	18 scalar + 2 Suo (C_{rr}=1.112, G=0.258)
v_0=0.33 (τ=10^{-3})	Joint (55–65) + 2.50 mm buffer	0.874	0.70	0.70 (6)	**1.16** (2)	**0.00**	[1.068, 1.080, 1.000, 1.000]
v_0=−0.80 (τ=10^{-3})	Boundary + 2.50 mm buffer	0.851	0.70	3.18 (5)	**5.52** (5)	**0.00**	[0.998, 1.110, 1.000, 1.000]
v_0=−0.80 (τ=10^{-4})	Boundary repair (0 mm buf)	0.900	0.70	9.57 (13)	73.98 (37)	116.40	[1.019, 1.127, 1.251, 1.395]
v_0=−0.80 (τ=10^{-4})	Boundary + 2.50 mm buffer	0.908	0.70	4.24 (6)	**8.13** (6)	**0.00**	[1.232, 1.427, 1.000, 1.000]

Background & Tolerance τ	Design strategy	$E_{max,C}$	h_{BD}/τ	Wide ring 55–65 mm (n^*)	Thin ring w=0.31 mm,K=64 (n^*)	Pressed-ring floor h_∞/τ	Outer 4 layers [a_{17}, a_{18}, a_{19}, a_{20}]
v_0=−0.80 (τ=10^{-4})	Joint (55–65) + 2.50 mm buffer	0.919	0.70	0.70 (6)	**2.29** (12)	**0.00**	[1.181, 1.245, 1.000, 1.000]

Table 5 | Unified T6 FE verification and physical performance of joint-repaired and geometry-tolerant bounded-stiffness designs

Design & Stiffness bounds	Hole geometry	Bound. disp. $\mathfrak{L}_{BD}$ (h/τ)	Poly. body force $\mathfrak{L}_{BF}$ (h/τ)	Wide ring 55–65 (h/τ)	Half ring 55–60 (h/τ)	Physical ratios R_{biax} | R_{ux} | R_{shear}	Worst-case E_{max}	Reaction / probe dev. ratio (ratio$_F$ | ratio$_s$) or ultrathin note
v_0=0.60 Joint-cloak (τ=10^{-3}, [0.02, 4.0])	Nominal (a_0=30 mm)	0.138	0.330	0.761	1.250	0.273 | 0.316 | 0.750	0.8402	—
v_0=0.60 Joint-cloak (τ=10^{-4}, [0.02, 4.0])	Nominal (a_0=30 mm)	0.071	0.428	0.763	2.520	0.636 | 0.656 | 0.850	0.9478	—
v_0=−0.80 Joint-cloak (τ=10^{-3}, [0.02, 4.0])	Nominal (a_0=30 mm)	0.543	0.400	0.648	0.902	0.525 | 0.841 | 0.828	0.8537	0.713 | 0.685 (8/8 physical loads < 1)
v_0=−0.80 Joint-cloak (τ=10^{-4}, [0.02, 4.0])	Nominal (a_0=30 mm)	0.536	0.209	0.682	1.281	0.834 | 0.909 | 0.907	0.9300	0.914 | 0.921
v_0=−0.80 Nominal-bounded ([0.71, 2.45])	Nominal (a_0=30 mm)	0.544	0.215	0.648	0.903	0.643 | 0.879 | 0.870	0.8955 (T6 0.8747)	—
v_0=−0.80 Nominal-bounded ([0.71, 2.45])	Shrunk (−1.5 mm hole)	0.478	**1.219** (fail)	**1.647** (fail)	**2.172** (fail)	0.619 | 0.885 | 0.876	0.8535 (T6 0.8341)	—
v_0=−0.80 Robust-bounded ([0.71, 2.45])	Nominal (a_0=30 mm)	0.543	0.151	0.213	0.293	0.657 | 0.886 | 0.879	0.9047 (+1.03%; T6 0.8816)	Ultrathin K=128: 0.977τ
v_0=−0.80 Robust-bounded ([0.71, 2.45])	Enlarged (+1.25 mm)	0.174	0.066	0.157	0.238	0.863 | 0.933 | 0.924	0.9880 (T6 0.9643)	—
v_0=−0.80 Robust-bounded ([0.71, 2.45])	Shrunk (−1.5 mm hole)	0.484	0.448	0.601	0.792	0.633 | 0.892 | 0.885	0.8620 (T6 0.8399)	—
v_0=−0.80 Robust-bounded ([0.71, 2.45])	Eccentric (1.5 mm offset)	0.549	0.138	0.308	0.426	0.740 | 0.904 | 0.900	0.9275 (T6 0.9070)	—
v_0=−0.80 Joint-cloak (τ=10^{-3}, [0.02, 4.0])	Enlarged (+1.25 mm)	—	—	—	—	0.908 | — | —	—	0.936 | 0.895
v_0=−0.80 Joint-cloak (τ=10^{-3}, [0.02, 4.0])	Shrunk (−1.5 mm hole)	—	—	—	—	0.499 | — | —	—	0.693 | 0.664
v_0=−0.80 Joint-cloak (τ=10^{-3}, [0.02, 4.0])	Eccentric (1.5 mm offset)	—	—	—	—	0.687 | — | —	—	0.834 | 0.892

Figure Captions

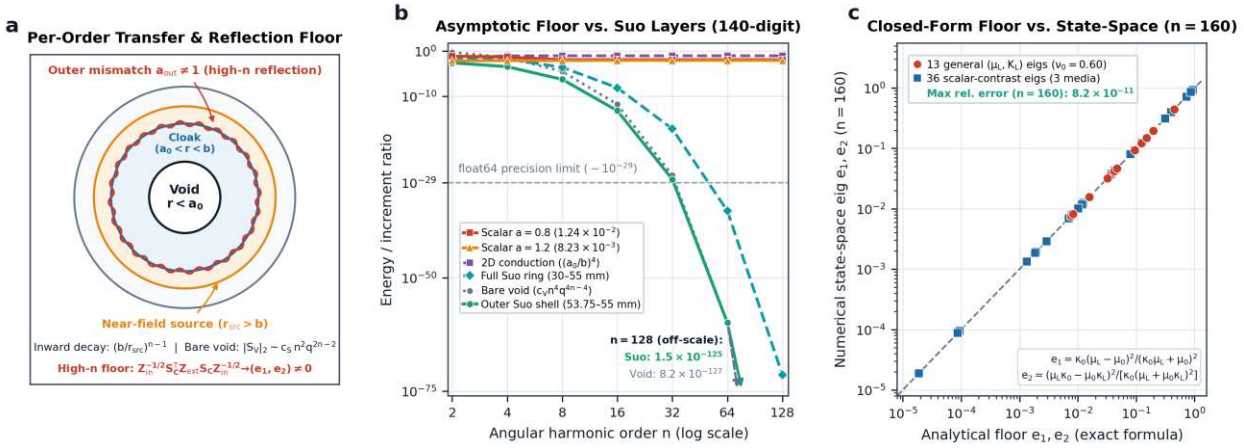


Figure 1 | Per-angular-order impedance theory, the exact high-order reflection floor, and the all-order neutral polar-orthotropic ring. a, Schematic of the per-order transfer geometry around a circular void ($r = a_0 = 30\text{mm}$) surrounded by a 20-layer cloak ($a_0 \le r \le b = 55\text{mm}$) in a plate of radius $R_{\text{out}} = 75\text{mm}$. Regular fields propagating inward from a source at $r_{\text{src}} > b$ decay as $(b/r_{\text{src}})^{n-1}$, and bare-hole scattering decays exponentially as $\|\boldsymbol{S}_V(n)\|_2 \sim c_S n^2 q^{2n-2} \to 0$ ($c_S = \kappa_0^{-1}(1-q^2)^2$, $q = a_0/b$). In contrast, any isotropic outer-edge mismatch $a_{\text{out}} \neq 1$ creates a non-vanishing flat-interface reflection floor (depicted schematically by the red short-wavelength ripple at $r = b$ for high angular order n), where the energy-weighted operator $\boldsymbol{Z}_{\text{in}}^{-1/2}\boldsymbol{S}_C^{\text{T}}\boldsymbol{Z}_{\text{ext}}\boldsymbol{S}_C\boldsymbol{Z}_{\text{in}}^{-1/2}$ approaches eigenvalues (e_1, e_2) as $n \to \infty$. **b**, Deterioration increment per unit incident-disc energy h_n^{inc} (cloak minus bare hole) over $n \in [2,128]$, computed in 140-digit arbitrary precision on $\nu_0 = 0.60$, shown alongside the non-incremental bare-hole baseline $\nu_n \sim \kappa_0^{-1}(1-q^2)^4 n^4 q^{4n-4}$ (dashed gray, with $c_V = \kappa_0^{-1}(1-q^2)^4$ and exponential rate $\lim_{n\to\infty} n^{-1}\ln\nu_n = 4\ln q$; it reaches 3.90×10^{-28} at $n = 32$ and drops below 10^{-75} to 8.18×10^{-127} at $n = 128$, as marked by downward off-scale arrows). Scalar outer layers ($a = 0.8, 1.2$) plateau at their analytical flat-interface floors (1.24×10^{-2} and 8.23×10^{-3}), and the closed-form 2D bilayer conduction cloak ($\sigma_L/\sigma_0 = 157/85$) plateaus at $(a_0/b)^4 \approx 8.85 \times 10^{-2}$ on the same incident-energy basis (corresponding to $h_\infty^{\text{cond}} = \frac{1}{2}(a_0/b)^4/\ell_V^{\text{cond}} = 1.7601$ under pressed-interface source input-energy normalization and bare-hole reference ℓ_V^{cond}). In contrast, a Suo-matched polar-orthotropic ring ($n_S = 1.2$, Equation 8) leaves $\mathcal{V}_\pm(n)$ invariant for all $n \ge 2$ ($h_\infty = 0$) while modifying internal radial exponents: replacing only the outermost 1.25mm layer ($53.75\text{–}55\text{mm}$, solid green) closely follows the bare hole down to $h_n^{\text{inc}} = 1.45 \times 10^{-125}$ at $n = 128$, whereas spanning the full $30\text{–}55\text{mm}$ annulus (dashed teal) decays at its modified exponent $p_-(n) \approx 0.5367n$ to 3.66×10^{-72} at $n = 128$. The IEEE-754 double-precision floor near 10^{-29} is indicated for reference. **c**, Parity plot comparing exact analytical reflection-floor eigenvalues (e_1, e_2) (Equation 5) against numerical energy-weighted state-space eigenvalues at $n = 160$ across 13 nonzero general isotropic (μ_L, K_L) eigenvalues (8 pairs on $\nu_0 = 0.60$, $\kappa_0 = 1.500$; red circles) and 36 scalar-contrast eigenvalues across all three media (blue squares), matching to a maximum relative error of 8.2×10^{-11} ($< 10^{-10}$).

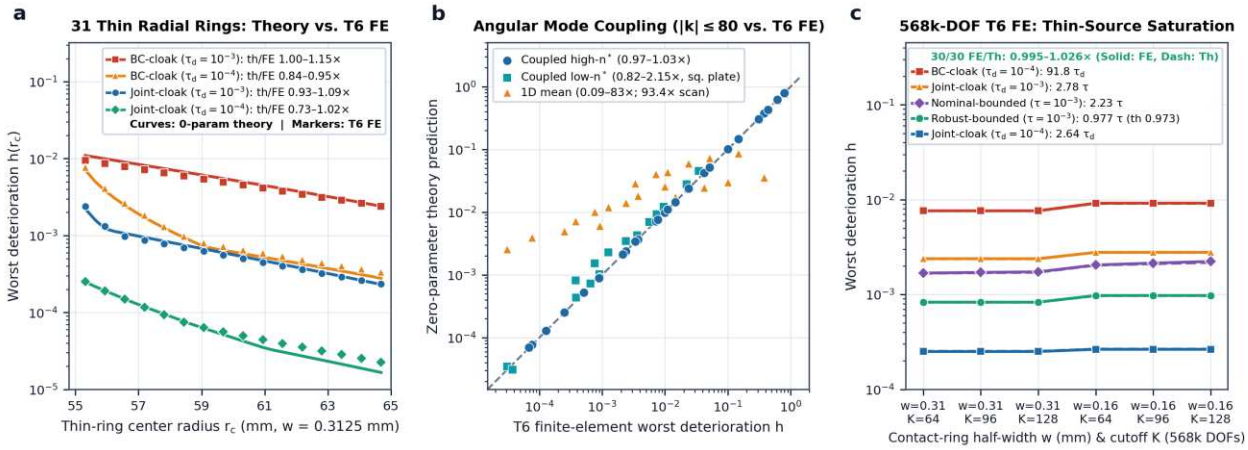


Figure 2 | Zero-parameter continuum and angularly coupled theory predicts independent T6 finite-element performance across radial scales. a, Radial profile of worst-case deterioration $h(r_c)$ across 31 thin radial rings ($r_c \in [55.31, 64.69]\text{mm}$, half-width 0.3125mm) in the auxetic medium ($\nu_0 = -0.80$), comparing zero-parameter axisymmetric continuum theory (curves) with T6 FE (markers) for BC-cloak and Joint-cloak designs at $\tau_d \in \{10^{-3}, 10^{-4}\}$ (0.73–1.15× agreement across all 31 rings). **b**, Comparison of angularly coupled theory ($|k| \le 80$) and 1D angle-averaged profiles (orange triangles, which deviate by 0.09–83× across the four benchmark radial classes and up to 93.4× on the 31-ring scan) across $\nu_0 \in \{0.60, 0.33, -0.80\}$. The coupled theory matches T6 FE within $0.97-1.03\times$ across all 27 high-n^* points (blue circles), while the 15 domain-sensitive low-n^* points ($n^* \le 14$, with 14/15 having $n^* \le 9$; teal squares) span $0.82-2.15\times$ owing to circular-versus-square outer plate geometry. **c**, High-resolution 567,938-DOF T6 FE verification across thin ($w = 0.3125\text{mm}$) and ultrathin ($w = 0.15625\text{mm}$) contact rings at angular cutoffs $K = 64, 96, 128$. Zero-parameter predictions (dashed) agree with T6 FE (solid with markers) within 0.995–1.026× across all 30 cases, with Robust-bounded on the nominal circle reaching 0.9768τ (6-pt) and 0.9757τ (150-pt) versus 0.973τ predicted.

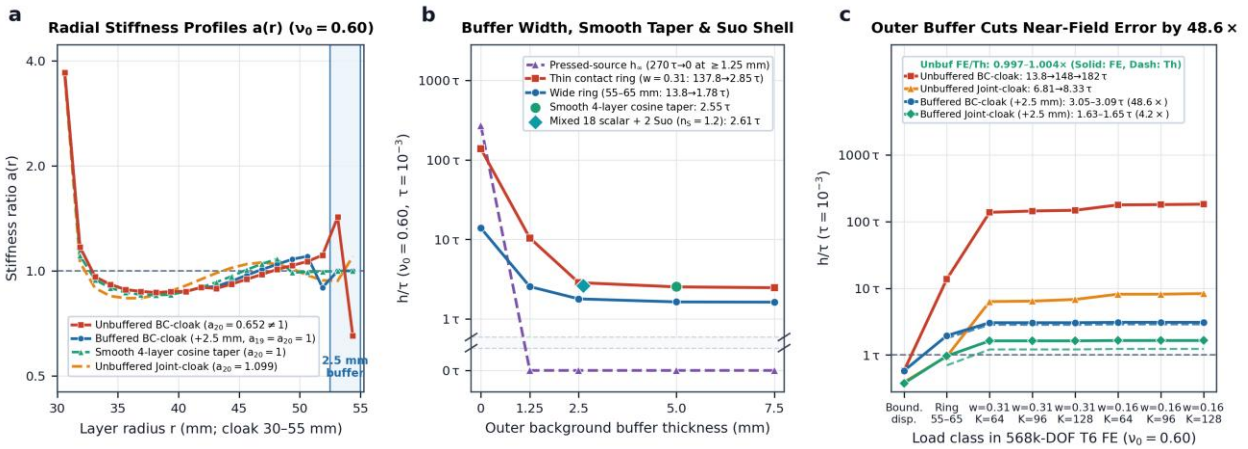


Figure 3 | Outer-edge impedance matching eliminates the high-order floor without near-field training. a, Radial stiffness profiles $a(r)$ across the 20 cloak layers ($30-55\text{mm}$) on $\nu_0 = 0.60$ ($\tau = 10^{-3}$) for the unbuffered BC-cloak ($a_{20} = 0.652$), buffered BC-cloak ($a_{19} = a_{20} = 1$, 2.5mm buffer), smooth 4-layer cosine taper, and unbuffered Joint-cloak ($a_{20} = 1.099$). **b**, Buffer-thickness scan ($0-7.5\text{mm}$) on $\nu_0 = 0.60$ with a broken vertical axis (// down to the exact 0τ baseline), showing collapse of the pressed-source floor h_∞ ($270\tau \to 0\tau$ at $\ge 1.25\text{mm}$), alongside results for the smooth 4-layer cosine taper ($h = 2.55\tau$) and the hybrid 18-scalar + 2-Suo-matched orthotropic shell ($n_S = 1.2$, $h = 2.61\tau$, $E_{\max,C} = 0.857$). **c**, Independent 567,938-DOF T6 FE verification comparing zero-parameter continuum predictions (dashed) against T6 FE (solid with markers) across 8 load classes. Adding a 2.5mm outer buffer reduces thin-contact ($w = 0.3125\text{mm}$, $K = 128$) deterioration by $48.6\times$ for boundary-only repair ($148.0\tau \to 3.05\tau$) and by $4.2\times$ for joint repair ($6.81\tau \to 1.63\tau$), stabilizing h across $K \in \{64, 96, 128\}$ and both hat widths (12/12 unbuffered FE/theory

ratios lie in 0.997–1.004×; buffered low-n^* square-versus-circular offsets are 1.08× and 1.34×, retaining a low-order residual of $3.05–3.09\tau > \tau$).

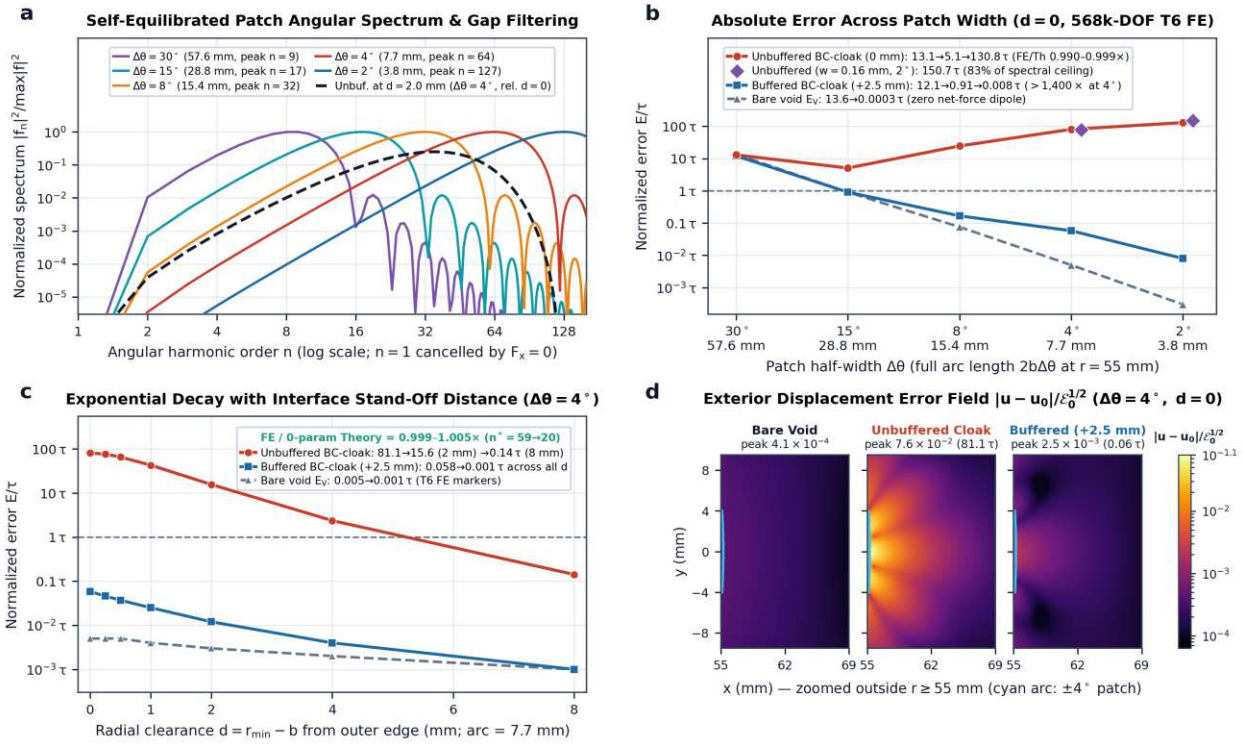


Figure 4 | Spatially localized finite-arc self-equilibrated force patches on fixed unbuffered and buffered BC-cloaks (567,938 DOFs, 150-point quadrature). a, Normalized angular power spectra $|\hat{f}_n|^2/\max|\hat{f}|^2$ (solid curves) of a single self-equilibrated patch supported on $|\theta| \le \Delta\theta \in [2^\circ, 30^\circ]$, illustrating exact cancellation of the $n = 1$ force mode and an upward spectral shift ($n_{\text{peak}} = 9 \to 127$) as the full arc width $2b\Delta\theta$ narrows ($57.6 \to 3.8\text{mm}$). The dashed black curve shows the normalized unbuffered scattering spectrum after stepping out to stand-off distance $d = 2.0\text{mm}$. **b**, Absolute normalized error energy $E/\tau = \mathcal{E}_{\text{err}}/(\mathcal{E}_0 \ell_V \tau)$ versus angular half-width at interface contact ($d = 0$, $w = 0.3125\text{mm}$). While bare-void error E_V drops steadily ($13.61\tau \to 0.0003\tau$), the unbuffered BC-cloak rises sharply from 5.11τ (15°) to 81.06τ (4°, $n^* = 59$) and 130.8τ (2°, $n^* = 98$), reaching 150.7τ at $w = 0.15625\text{mm}$ (purple diamonds). By contrast, the $+2.5\text{mm}$ Buffered BC-cloak stays within $0.008–0.911\tau$ (a $> 1{,}400\times$ reduction at 4°), with zero-parameter theory matching T6 FE within 0.990–0.999× for $\Delta\theta \le 15^\circ$. **c**, Exponential decay with stand-off clearance $d = r_{\min} - b \in [0,8]\text{mm}$ for a fixed $\Delta\theta = 4^\circ$ (7.7mm arc) patch: the unbuffered cloak decays monotonically from 81.06τ ($n^* = 59$) through 15.64τ (2mm) to 0.142τ (8mm, $n^* = 20$), matching zero-parameter theory within 0.999–1.005×, whereas the buffered cloak remains $\le 0.058\tau$ throughout. **d**, Real-space 2D exterior displacement error magnitude $|\boldsymbol{u} - \boldsymbol{u}_0|/\sqrt{\mathcal{E}_0}$ outside $r = 55\text{mm}$ near the $\pm 4^\circ$ contact patch (cyan arc), plotted on a common logarithmic color scale. The unbuffered cloak emits intense multi-lobe high-harmonic interface ripples (peak 7.6×10^{-2}), which the $+2.5\text{mm}$ buffer suppresses by $30\times$ (to 2.5×10^{-3}, approaching the bare-void peak of 4.1×10^{-4}).

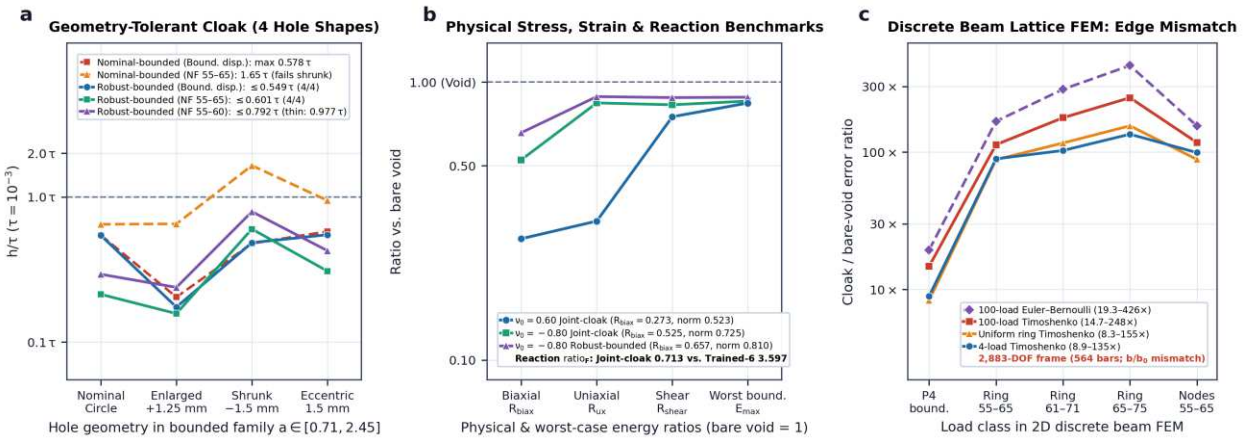


Figure 5 | Constructive geometry-tolerant bounded-stiffness design, physical benchmarks, and direct 2D discrete-beam lattice FEM verification. a, Independent T6 FE verification of Nominal-bounded (dashed, failing the $55-65\text{mm}$ ring at 1.65τ on the shrunk hole) versus Robust-bounded (solid) within the bounded stiffness range $a \in [0.71,2.45]$ across four hole geometries (nominal circle, $+1.25\text{mm}$ enlarged, -1.5mm shrunk, and 1.5mm eccentric). Robust-bounded satisfies $h \le 0.549\tau$ (boundary displacement), $h \le 0.601\tau$ $(55-65\text{mm})$, and $h \le 0.792\tau$ $(55-60\text{mm})$ across all four shapes at only +1.03% nominal boundary cost. **b**, Physical mechanics benchmarks for joint designs: $\nu_0 = 0.60$ Joint-cloak ($R_{\text{biax}} = 0.273$, norm 0.523, $R_{\text{ux}} = 0.316$, $R_{\text{shear}} = 0.750$), $\nu_0 = -0.80$ Joint-cloak ($R_{\text{biax}} = 0.525$, norm 0.725, $R_{\text{ux}} = 0.841$, $R_{\text{shear}} = 0.828$, reaction ratio $\text{ratio}_F = 0.713$ vs. Trained-6 3.597), and Robust-bounded ($R_{\text{biax}} = 0.657$, norm 0.810, $R_{\text{ux}} = 0.886$, $R_{\text{shear}} = 0.879$). **c**, Direct 2D discrete Timoshenko ($k_s = 5/6$, solid curves) and Euler–Bernoulli (dashed purple) beam finite-element results (961 nodes, 2,883 DOFs, 564 cloak bars; $\ell = 4.839\text{mm}$, $b_0 = 0.938\text{mm}$) for the 100-load, uniform, and 4-load square lattices across P_4 boundary loads, near-field rings $(55-65, 61-71, 65-75\text{mm})$, and all discrete exterior nodes in $55-65\text{mm}$. Both models confirm an order-of-magnitude near-field error jump (8.3–14.7× on boundary loads to 87.9–248.2× in the near field for Timoshenko beams; 19.3–425.8× for the 100-load Euler–Bernoulli model; 10.2–19.3× to 92.5–425.8× across all three Euler–Bernoulli lattices).

References

1. Pendry, J. B., Schurig, D. & Smith, D. R. Controlling electromagnetic fields. *Science* **312**, 1780–1782 (2006).
2. Leonhardt, U. Optical conformal mapping. *Science* **312**, 1777–1780 (2006).
3. Milton, G. W., Briane, M. & Willis, J. R. On cloaking for elasticity and physical equations with a transformation invariant form. *New J. Phys.* **8**, 248 (2006).
4. Norris, A. N. Acoustic cloaking theory. *Proc. R. Soc. A* **464**, 2411–2434 (2008).
5. Brun, M., Guenneau, S. & Movchan, A. B. Achieving control of in-plane elastic waves. *Appl. Phys. Lett.* **94**, 061903 (2009).
6. Farhat, M., Guenneau, S. & Enoch, S. Ultrabroadband elastic cloaking in thin plates. *Phys. Rev. Lett.* **103**, 024301 (2009).
7. Norris, A. N. & Shuvalov, A. L. Elastic cloaking theory. *Wave Motion* **48**, 525–538 (2011).
8. Stenger, N., Wilhelm, M. & Wegener, M. Experiments on elastic cloaking in thin plates. *Phys. Rev. Lett.* **108**, 014301 (2012).
9. Bückmann, T., Thiel, M., Kadic, M., Schittny, R. & Wegener, M. An elasto-mechanical unfeelability cloak made of pentamode metamaterials. *Nat. Commun.* **5**, 4130 (2014).
10. Bückmann, T., Kadic, M., Schittny, R. & Wegener, M. Mechanical cloak design by direct lattice transformation. *Proc. Natl. Acad. Sci. U.S.A.* **112**, 4930–4934 (2015).
11. Bertoldi, K., Vitelli, V., Christensen, J. & van Hecke, M. Flexible mechanical metamaterials. *Nat. Rev. Mater.* **2**, 17066 (2017).

12. Kadic, M., Milton, G. W., van Hecke, M. & Wegener, M. 3D metamaterials. *Nat. Rev. Phys.* **1**, 198–210 (2019).

13. Fachinotti, V. D., Peralta, I. & Albanesi, A. E. Optimization-based design of an elastostatic cloaking device. *Sci. Rep.* **8**, 9857 (2018).

14. Senhora, F. V., Sanders, E. D. & Paulino, G. H. Optimally-tailored spinodal architected materials for multiscale design and manufacturing. *Adv. Mater.* **34**, 2109304 (2022).

15. Wang, L. et al. Mechanical cloak via data-driven aperiodic metamaterial design. *Proc. Natl. Acad. Sci. U.S.A.* **119**, e2122185119 (2022).

16. Cheng, X. et al. A compatible boundary condition-based topology optimization paradigm for static mechanical cloak design. *Extreme Mech. Lett.* **65**, 102100 (2023).

17. Yang, Z. et al. Static mechanical cloaking and camouflage from disorder. *Nat. Commun.* **16**, 8858 (2025).

18. Senhora, F. V., Sanders, E. D. & Paulino, G. H. Unbiased mechanical cloaks. *Proc. Natl. Acad. Sci. U.S.A.* **122**, e2415056122 (2025).

19. Monticone, F. & Alù, A. Do cloaked objects really scatter less? *Phys. Rev. X* **3**, 041005 (2013).

20. Alù, A. & Engheta, N. Achieving transparency with plasmonic and metamaterial coatings. *Phys. Rev. E* **72**, 016623 (2005).

21. Greenleaf, A., Lassas, M. & Uhlmann, G. On nonuniqueness for Calderón's inverse problem. *Math. Res. Lett.* **10**, 685–693 (2003).

22. Kohn, R. V., Shen, H., Vogelius, M. S. & Weinstein, M. I. Cloaking via change of variables in electric impedance tomography. *Inverse Probl.* **24**, 015016 (2008).

23. Ammari, H., Kang, H., Lee, H. & Lim, M. Enhancement of near cloaking using generalized polarization tensors vanishing structures. Part I: The conductivity problem. *Commun. Math. Phys.* **317**, 253–266 (2013).

24. Hashin, Z. The elastic moduli of heterogeneous materials. *J. Appl. Mech.* **29**, 143–150 (1962).

25. Ru, C. Q. Interface design of neutral elastic inclusions. *Int. J. Solids Struct.* **35**, 559–572 (1998).

26. Benveniste, Y. & Miloh, T. Neutral inhomogeneities in conduction phenomena. *J. Mech. Phys. Solids* **47**, 1873–1892 (1999).

27. Milton, G. W. & Serkov, S. K. Neutral coated inclusions in conductivity and anti-plane elasticity. *Proc. R. Soc. Lond. A* **457**, 1973–1997 (2001).

28. Norris, A. N. & Parnell, W. J. Static elastic cloaking, low-frequency elastic wave transparency and neutral inclusions. *Proc. R. Soc. A* **476**, 20190725 (2020).

29. Norris, A. N. & Parnell, W. J. Hyperelastic cloaking theory: transformation elasticity with pre-stressed solids. *Proc. R. Soc. A* **468**, 2881–2903 (2012).

30. Schittny, R., Kadic, M., Guenneau, S. & Wegener, M. Experiments on transformation thermodynamics: molding the flow of heat. *Phys. Rev. Lett.* **110**, 195901 (2013).

31. Han, T. et al. Experimental demonstration of a bilayer thermal cloak. *Phys. Rev. Lett.* **112**, 054302 (2014).

32. Zhang, Z. et al. Diffusion metamaterials. *Nat. Rev. Phys.* **5**, 218–235 (2023).

33. Stroh, A. N. Dislocations and cracks in anisotropic elasticity. *Philos. Mag.* **3**, 625–646 (1958).

34. Barnett, D. M. & Lothe, J. Synthesis of the sextic and the integral formalism for dislocations, Green's functions, and surface waves in anisotropic elastic solids. *Phys. Norvegica* **7**, 13–19 (1973).

35. Suo, Z. Singularities, interfaces and cracks in dissimilar anisotropic media. *Proc. R. Soc. Lond. A* **427**, 331–358 (1990).

36. Ting, T. C. T. *Anisotropic Elasticity: Theory and Applications* (Oxford Univ. Press, 1996).

37. Lakes, R. Foam structures with a negative Poisson's ratio. *Science* **235**, 1038–1040 (1987).

38. Dundurs, J. Discussion of "Edge-bonded dissimilar orthogonal elastic wedges under normal and shear loading". *J. Appl. Mech.* **36**, 650–652 (1969).

39. Bourdin, B. Filters in topology optimization. *Int. J. Numer. Methods Eng.* **50**, 2143–2158 (2001).

40. Sigmund, O. & Maute, K. Topology optimization approaches: a comparative review. *Struct. Multidiscip. Optim.* **48**, 1031–1055 (2013).

41. Liu, D. C. & Nocedal, J. On the limited memory BFGS method for large scale optimization. *Math. Program.* **45**, 503–528 (1989).